University of Southern Denmark

Center for Polariton-driven Light-Matter Interactions

Toward Axion Detection in the THz Region Using Graphene Nanostructures

Master's Thesis

Thesis submitted by

Viktor Damsgaard Skarby
viska21@student.sdu.dk

Thesis Advisors:

Prof. Joel D. Cox
cox@mci.sdu.dk

Dr. Eduardo J. C. Dias
dias@mci.sdu.dk

Assoc. Prof. Manuel Meyer
mey@sdu.dk

Department of Physics, Chemistry and Pharmacy
University of Southern Denmark - Odense
June 1 2026

Abstract

The detection of axions is a field of high interest in high-energy physics and cosmology, since these hypothetical particles are promising candidates potentially able to solve both the dark matter and strong CP problems. However, the mass of these axions is predicted to be incredibly small, and they interact very weakly with light and matter, making it challenging to find them. Past and current experiments have continuously ruled out different combinations of mass and axion–light coupling, but a lot of the available phase space remains unexplored, motivating the need for new detection schemes. In particular, the region around a few THz of axion mass has so far escaped exploration.

In this thesis, we examine the possibilities of using graphene plasmonic nanostructures as detection platforms for axions. Graphene is a 2D material that, when doped, acts as a metal, supporting optical resonances in the THz frequency range known as surface polaritons. We devise graphene-based nanostructures, complemented by additional elements such as gold or small scatterers, that can respond optically to the axion fields and trigger their conversion into detectable photons.

We first review the classical electrodynamics used to describe graphene plasmonics. Using the Green's function formalism, we develop a framework to describe multilayered nanostructures. Using the axion-modified Maxwell equations, we find that, when in the presence of a strong magnetic field, the axions act as a classical current. This can then be combined with our established theory to finally calculate the enhanced photon count of stacks of extended graphene sheets or ribbons.

Our estimates predict that the photon counts in the extended graphene geometry yields an emission rate of $\Gamma_{\text{count}} = 10^{-35}$ photons per second. This result can be improved considerably by using confined systems, such as graphene ribbons. We estimate an enhancement of 9 orders of magnitude, compared to similarly doped graphene sheets, when using a ribbon with a width of $W = 1$ μm and a length of $L = 100$ μm. Finally, we discuss various ways to improve upon these results, in order to make viable detection systems.

Resumé

Detektionen af axioner er et område af stor interesse i højenergifysik og kosmologi, da de disse hypotetiske partikler er lovende kandidater til potentielt at løse både mørkstof og det stærke CP problem. Det forudsiges dog, at axioners masse er utrolig lille og at de interagerer meget svagt med lys og stof, hvilket gør det svært at finde dem. Både tidligere og nuværende eksperimenter har forsat udelukket forskellige kombinationer af masse og axionlys kobling, men en stor del af fase rummet er stadig uudforsket, hvilket motivere nødvendigheden for detektions eksperimenter. Især er området omkring et par THz af axion massen hidtil ikke blevet undersøgt.

I denne afhandling, undersøger vi muligheden for at bruge grafen baseret plasmoniske nanostrukturer som detektions platforme for axioner. Grafen er et 2D materiale som, når det er dopede, fungere som et metal, der kan understøtte optiske resonanser i THz området, kendt som overflade polaritoner. Vi udvikler nanostrukturer baseret på grafen, suppleret med yderligere elementer såsom guld eller små scatterers, som kan reagere optisk på axionfelterne og udløse deres omdannelse til detekterbare fotoner.

Vi gennemgår først den klassiske elektrodynamik, der anvendes til at beskrive grafen plasmoner. Ved hjælp af Greens-funktions formalismen udvikler vi metoder til beskrivelse af flerlagede nanostrukturer. Ved hjælp af de axion-modificerede Maxwell-ligninger finder vi, at axionerne i et stærkt magnetfelt opfører sig som en klassisk strøm. Dette kan derefter kombineres med vores etablerede teori for endelig at beregne det forhøjede fotontal for stakke af udstrakte grafenplader eller -bånd.

Vores estimater forudsiger en foton rate på $\Gamma_{\text{count}} = 10^{-35}$ per sekund, for systemet med stakke af udstrakte grafenplader. Dette resultat kan blive yderligere forbedret ved i stedet at bruge lukkede systemer, såsom grafenbånd. Vi anslår en forbedring på 9 størrelsesordener i forhold til grafenplader med tilsvarende doping, når der anvendes et bånd med bredden $W = 1$ μm og længden $L = 100$ μm. Til sidst diskuterer vi forskellige måder, hvorpå disse resultater kan forbedres, med henblik på at udvikle brugbare detektionssystemer.

Acknowledgements

I want to extend my gratitude to Joel and Manuel for their insight, help, and company during this project, it has been a pleasure working with you. A special thanks to Eduardo for the many hours of discussion and guidance. I have greatly valued our meetings, which were both engaging and highly educational. Finally, thank you to the POLIMA group for hosting me during this project. It has been a very pleasant environment to study and learn in.

Contents

Abstract i

Resumé ii

Acknowledgements iii

1 Introduction v

2 Classical Electrodynamics 2
- 2.1 Maxwell's Equations . . . 2
  - 2.1.1 Time-Harmonic Fields . . . 3
  - 2.1.2 Boundary Conditions and Fresnel Coefficients . . . 3
- 2.2 Graphene Nanophotonics . . . 7
  - 2.2.1 Optical Conductivity of Graphene . . . 8
- 2.3 Surface-Plasmon Polaritons . . . 9
  - 2.3.1 Graphene Plasmons . . . 11
- 2.4 Green's Functions . . . 17
  - 2.4.1 Green's Function for Stratified Media . . . 18
  - 2.4.2 The Field of a Point Dipole . . . 21
  - 2.4.3 Green's Function for Spatially Uniform Source . . . 25

3 Axion Electrodynamics 28
- 3.1 Modified Maxwell Equations . . . 29
  - 3.1.1 Axions as Photon Sources . . . 30
- 3.2 Axions in Nanophotonics . . . 31
  - 3.2.1 Axion Detection in Extended Systems . . . 32
  - 3.2.2 Axion Detection in Confined Systems . . . 35
  - 3.2.3 Possible Directions for Count Improvement . . . 36

4 Conclusion 38

A Transfer Matrices for Stratified Media 39
- A.1 Phase Safe TMM . . . 41

Declaration of AI use 44

Chapter 1

Introduction

In 1976 it was shown by G. 't Hooft [1] that strong interactions in principle allow for the breaking of both the charge conjugation and parity symmetries, known as CP-violation, resulting in a large dipole moment of the neutron. However, the opposite was shown by experiment, which found the CP symmetry to be preserved to a high degree [2]. The apparent conservation of the CP symmetry in strong interactions is known as the strong CP problem. Shortly after the appearance of this problem, R. Peccei and H. Quinn showed that the addition of a new, spontaneously broken, global symmetry, known as the Peccei-Quinn symmetry, would remove the CP-violating terms in the strong interaction, effectively solving the issue [3]. It was then shown, independently, by S. Weinberg and F. Wilczek that this would result in a Goldstone boson, which Wilczek named the *axion* [4, 5].

Initially, the axion was not the focus among particle physicists, who focused on high-energy physics, searching for the Higgs boson, and in parallel for WIMPs (Weakly Interacting Massive Particles), one of the initial candidates for solving dark matter [6]. However, it was later shown that axions may also constitute the dark matter that seems to dominate our universe, since they can be long-lived and weakly interacting [7]. As such, axions may now solve two pressing problems of modern physics, and have therefore gained more experimental efforts in recent years.

In this work, we will explore the possibility of detecting axions in a nanophotonic environment, specifically utilizing the enhancement provided by graphene plasmons at the THz frequency range. In Chapter 2 we first review the necessary classical electrodynamics followed by an introduction to the optical properties of graphene. We then examine the features of surface-plasmon polaritons in both extended gold and graphene, highlighting the differences between traditional metals and graphene. We also include a small section on graphene ribbons, which, in contrast to extended graphene sheets, support multiple modes and can be directly excited by light. We then finish the chapter with a section on Green's functions, introducing a general formalism for extended stratified media, allowing us to calculate the electric field of sources embedded in multilayered strictures. Having established a strong foundation, we proceed to introduce the axion in Chapter 3 and derive the axion modified Maxwell equations. From these we show that, given a strong magnetic field, axions can be viewed as classical photon sources that can be incorporated directly into the Green's function formalism. Finally, we examine how

different nanostructures enhance the photon count, the influence of graphene doping, the possible use of graphene ribbons and potential ways to the improve photon count. In Chapter 4 we summarize the thesis and discuss the final results.

Chapter 2

Classical Electrodynamics

In this chapter, we review the physics of classical electrodynamics that are the basis of the optical procedure to detect axions explored in this thesis. Here, we omit the modification of electrodynamics due to the presence axions, which is addressed in Chapter 3. Throughout the thesis we use SI units.

2.1 Maxwell's Equations

Given some free charge and current density distributions $\rho(\mathbf{r}, t)$ and $\mathbf{j}(\mathbf{r}, t)$ at position $\mathbf{r}$ and time t, the dynamics of the electromagnetic fields are governed by the macroscopic Maxwell's equations

$$\nabla \cdot \mathbf{D}(\mathbf{r}, t) = \rho(\mathbf{r}, t), \tag{2.1a}$$
$$\nabla \cdot \mathbf{B}(\mathbf{r}, t) = 0, \tag{2.1b}$$
$$\nabla \times \mathbf{E}(\mathbf{r}, t) = -\partial_t \mathbf{B}(\mathbf{r}, t), \tag{2.1c}$$
$$\nabla \times \mathbf{H}(\mathbf{r}, t) = \mathbf{j}(\mathbf{r}, t) + \partial_t \mathbf{D}(\mathbf{r}, t), \tag{2.1d}$$

where $\mathbf{E}$ is the electric field, $\mathbf{D}$ is the displacement field, $\mathbf{B}$ is the magnetic induction and $\mathbf{H}$ is the magnetic field. From these we can derive the related continuity equation

$$\nabla \cdot \mathbf{j}(\mathbf{r}, t) = -\partial_t \rho(\mathbf{r}, t), \tag{2.2}$$

ensuring the conservation of charge. Equations (2.1) do not form a closed set of equations, meaning we must introduce a pair of constitutive relations that connect $\mathbf{D}$, $\mathbf{H}$ with the true fields $\mathbf{E}$, $\mathbf{B}$. Assuming that the media the fields propagate through are linear, isotropic and local, these relations are

$$\mathbf{D} = \varepsilon \mathbf{E}, \tag{2.3a}$$
$$\mathbf{H} = \frac{1}{\mu} \mathbf{B}, \tag{2.3b}$$

where we have introduced the material dependent permittivity $\varepsilon = \varepsilon_\mathrm{r} \varepsilon_0$ and permeability $\mu = \mu_\mathrm{r} \mu_0$, which are characterized by their relative values ε_r and μ_r with respect to the

vacuum ones ε_0 and μ_0, respectively. With these, the inhomogeneous wave equation can derived by taking the curl of Eqs. (2.1c) and (2.1d), leading to

$$\left(\nabla^2 - \varepsilon\mu\partial_t^2\right)\mathbf{E}^2(\mathbf{r},t) = \mu\partial_t\mathbf{j}(\mathbf{r},t) + \frac{1}{\varepsilon}\nabla\rho(\mathbf{r},t), \tag{2.4a}$$

$$\left(\nabla^2 - \varepsilon\mu\partial_t^2\right)\mathbf{H}(\mathbf{r},t) = -\nabla\times\mathbf{j}(\mathbf{r},t). \tag{2.4b}$$

2.1.1 Time-Harmonic Fields

We assume that all fields oscillate with a single frequency ω such that the time dependence of $\mathbf{E}$ can be written as

$$\mathbf{E}(\mathbf{r},t) = \mathbf{E}(\mathbf{r},\omega)\mathrm{e}^{-\mathrm{i}\omega t} + \mathbf{E}^*(\mathbf{r},\omega)\mathrm{e}^{\mathrm{i}\omega t}, \tag{2.5}$$

and similarly for the other fields. Note that while $\mathbf{E}(\mathbf{r},t)$ is real, the frequency-domain counterpart $\mathbf{E}(\mathbf{r},\omega)$ is complex. For time-harmonic fields, the homogeneous wave equation becomes

$$\left(\nabla^2 + k^2\right)\mathbf{E}(\mathbf{r},\omega) = 0, \quad k^2 = \omega^2/c'^2, \tag{2.6}$$

where

$$c' = \frac{c}{n} = \frac{c}{\sqrt{\varepsilon_\mathrm{r}\mu_r}}, \tag{2.7}$$

is the speed of light in a medium characterized by the refractive index $n = \sqrt{\varepsilon_\mathrm{r}\mu_r}$. Equation (2.6) has a trivial plane wave solution of the form

$$\mathbf{E}(\mathbf{r},\omega) = \mathbf{E}_0(\omega)\mathrm{e}^{\mathrm{i}\mathbf{k}\cdot\mathbf{r}}, \tag{2.8}$$

where $\mathbf{k} = (k_x, k_y, k_z)$ is the field's wavevector, related to its frequency through $|\mathbf{k}| = k = \omega/c'$. The electric field in the time domain can then be written as

$$\mathbf{E}(\mathbf{r},t) = \mathbf{E}_0(\omega)\mathrm{e}^{\mathrm{i}(\mathbf{k}\cdot\mathbf{r}-\omega t)} + \text{c.c.}, \tag{2.9}$$

where c.c. is the complex conjugate of the preceding term, and analogously for $\mathbf{H}(\mathbf{r},t)$.

2.1.2 Boundary Conditions and Fresnel Coefficients

In practice, we often consider systems consisting of more than one material, and, as such, we must ensure that the fields are continuous when going from one medium to another. This is guaranteed through a set of boundary conditions, which can be derived from the Maxwell equations in their integral representation [8].

Labeling the two media as 1 and 2, as shown in Fig. 2.1, the fields must, locally at any interface, obey the following relations

$$\hat{\mathbf{n}}\times(\mathbf{E}_1 - \mathbf{E}_2) = 0, \tag{2.10a}$$

$$\hat{\mathbf{n}}\times(\mathbf{H}_1 - \mathbf{H}_2) = \mathbf{j}_s, \tag{2.10b}$$

$$\hat{\mathbf{n}}\cdot(\mathbf{D}_1 - \mathbf{D}_2) = \rho_s, \tag{2.10c}$$

$$\hat{\mathbf{n}}\cdot(\mathbf{B}_1 - \mathbf{B}_2) = 0, \tag{2.10d}$$

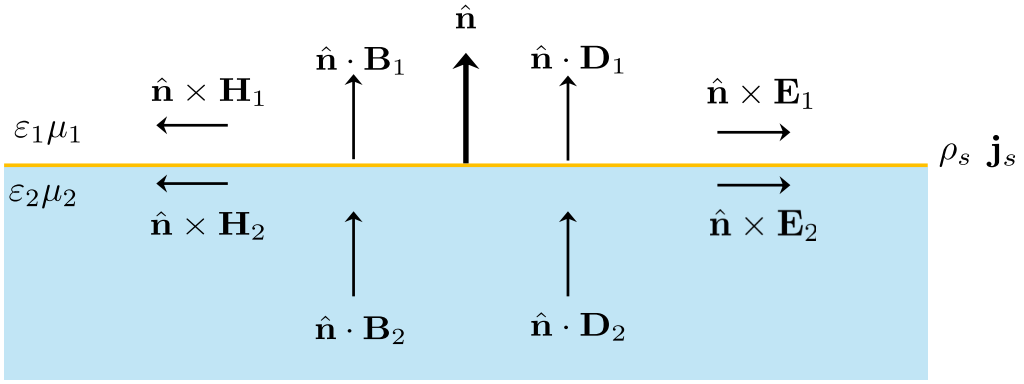

Figure 2.1: Illustration of an interface between two different media, the first one being characterized by ε_1, μ_1 and the the second one by ε_2, μ_2. The normal vector, $\hat{\mathbf{n}}$, is defined as going from medium 2 to 1. Notice how the equations involving the cross product describe the continuity of the parallel components of the fields, while the equations with the dot product do so for the perpendicular components. Possible surface charge and current densities are represented by ρ_s and $\mathbf{j}_s$, respectively.

where $\hat{\mathbf{n}}$ is a unit normal vector on the interface pointing from medium 2 to 1. Furthermore, we have accounted for possible surface charges (ρ_s) and currents ($\mathbf{j}_s$) at the interface. These would present e.g. if we included a 2D material at the boundary.

From these boundary conditions, we can readily derive the Fresnel reflection and transmission coefficients that characterize the scattering of a plane wave by a planar surface. In the presence of a system with in-plane translational symmetry, we can write some arbitrarily polarized wave of the form $\mathbf{E}_0 \exp[\mathrm{i}(\mathbf{k}\cdot\mathbf{r} - \omega t)]$, as a combination of two orthogonally polarized waves: $\mathbf{E}_0 = \mathbf{E}_0^{(\mathrm{s})} + \mathbf{E}_0^{(\mathrm{p})}$. Here, $\mathbf{E}_0^{(\mathrm{s})}$ is parallel to the surface, labeled (s) or sometimes TE (transverse electric), while $\mathbf{E}_0^{(\mathrm{p})}$ is perpendicular to the wavevector $\mathbf{k}$ and $\mathbf{E}_0^{(\mathrm{s})}$, labeled either (p) or TM (transverse magnetic) [9], as shown in Fig. 2.2. We consider the system depicted in Fig. 2.2, where an incoming wave impinges on an interface between two different media. From the homogeneous wave equation, we know that the wave is characterized by the wavevectors

$$\mathbf{k}_j = (k_x, k_y, k_{zj}), \quad |\mathbf{k}_j| = \omega/c_j' = \sqrt{k_x^2 + k_y^2 + k_{zj}^2}, \tag{2.11}$$

where the index j indicates the material. The z component is then given by

$$k_{zj} = \sqrt{\omega^2/c_j'^2 - k_\parallel^2}, \quad \text{where} \quad k_\parallel^2 = k_x^2 + k_y^2, \tag{2.12}$$

since we consider an extended surface, such that we have translational invariance in the x and y directions. The s-polarized fields are then given by

$$\mathbf{E}_1^{(\mathrm{s})} = E_0^{(\mathrm{s})}\left(\mathrm{e}^{-\mathrm{i}k_{z1}z} + r^{(\mathrm{s})}\mathrm{e}^{\mathrm{i}k_{z1}z}\right)\hat{\mathbf{y}}, \tag{2.13a}$$

$$\mathbf{E}_2^{(\mathrm{s})} = E_0^{(\mathrm{s})} t^{(\mathrm{s})}\mathrm{e}^{-\mathrm{i}k_{z2}z}\hat{\mathbf{y}} \tag{2.13b}$$

where an $\exp\left[\mathrm{i}\left(k_\parallel x - \omega t\right)\right]$ dependence is implicit for both fields. The first field consists of both an incoming and outgoing (reflected) wave, while in the second material there is

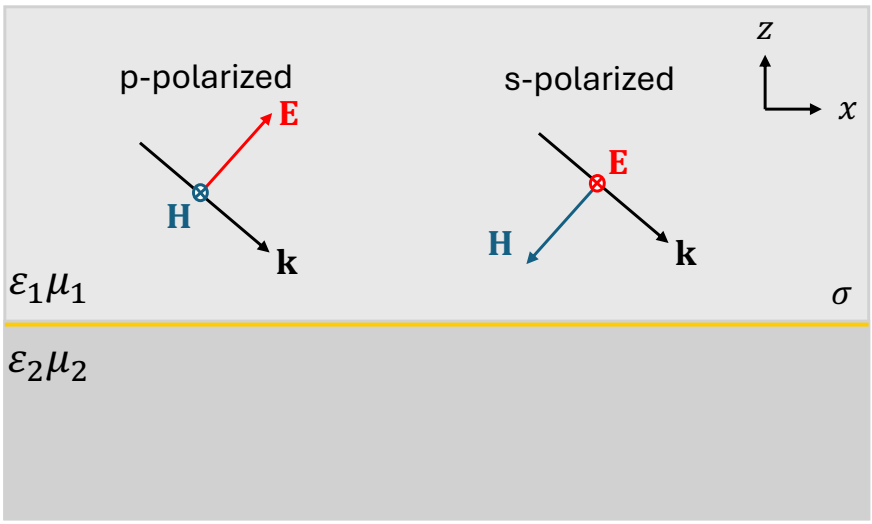

Figure 2.2: The difference between p-polarized light (the **H** field is parallel to the interface) and s-polarized light (the **E** field is parallel to the interface). We account for possible surface charges at the interface with the surface conductivity σ_s.

only a transmitted part. Now, using Faraday's law along Eqs. (2.10a) and (2.10b), we can derive the reflection and transmission coefficients

$$r^{(\mathrm{s})} = \frac{k_{z1}\mu_2 - k_{z2}\mu_1 - \mu_1\mu_2\omega\sigma}{k_{z1}\mu_2 + k_{z2}\mu_1 + \mu_1\mu_2\omega\sigma}, \tag{2.14a}$$

$$t^{(\mathrm{s})} = \frac{2k_{z1}\mu_2}{k_{z1}\mu_2 + k_{z2}\mu_1 + \mu_1\mu_2\omega\sigma}, \tag{2.14b}$$

where we have used Ohm's law to relate the surface current to an isotropic surface conductivity σ describing the surface charges,

$$\mathbf{j}_s = \sigma\mathbf{E}. \tag{2.15}$$

An almost identical approach can be applied to get the p-polarized Fresnel coefficients

$$r^{(\mathrm{p})} = \frac{k_{z1}\varepsilon_2 - k_{z2}\varepsilon_1 + k_{z1}k_{z2}\sigma/\omega}{k_{z1}\varepsilon_2 + k_{z2}\varepsilon_1 + k_{z1}k_{z2}\sigma/\omega}, \tag{2.16a}$$

$$t^{(\mathrm{p})} = \frac{2k_{z1}\varepsilon_2}{k_{z1}\varepsilon_2 + k_{z2}\varepsilon_1 + k_{z1}k_{z2}\sigma/\omega}\frac{Z_2}{Z_1}, \tag{2.16b}$$

where $Z_j = \sqrt{\mu_j/\varepsilon_j}$ is the wave impedance.

The Fresnel coefficients describe how much of the field amplitudes are reflected/transmitted. However, in practice, we almost always measure the energy of the fields, which correspond to the reflectance and transmittance

$$\mathcal{R}^{(\nu)} = \left|r^{(\nu)}\right|^2, \tag{2.17a}$$

$$\mathcal{T}^{(\nu)} = \frac{\mu_1\mathrm{Re}\{k_{z2}\}}{\mu_2\mathrm{Re}\{k_{z1}\}}\left|t^{(\nu)}\right|^2, \tag{2.17b}$$

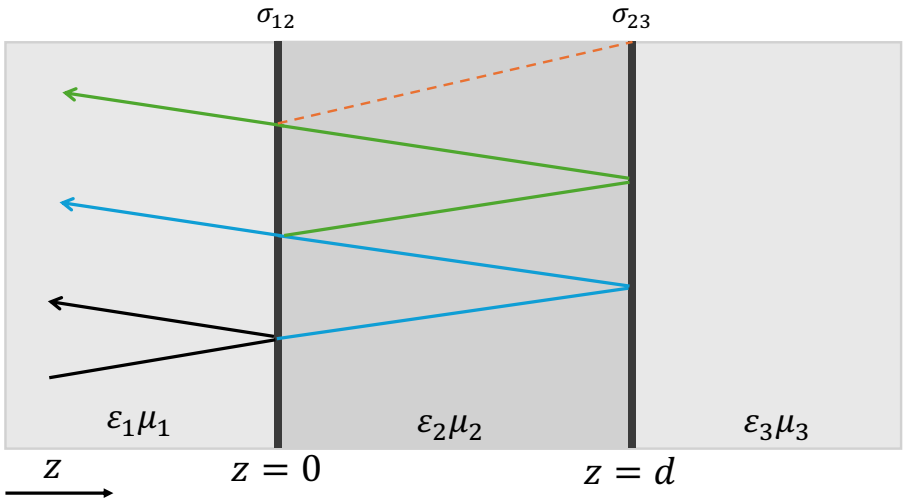

Figure 2.3: Schematic of a three-layer system, with the incident field impinging from the first interface side. The arrows of different colors denote different contributions to the overall reflected field through a different number of internal reflections. σ_{12} and σ_{23} account for possible surface charges.

where $\nu = \mathrm{s}, \mathrm{p}$ indicates the polarization.

Next, we consider a 3-layered system, as depicted in Fig. 2.3. Unlike the single interface case, here the reflected field from the layered structure accounts for the direct reflection when crossing from medium 1 to 2, but also all remaining contributions arising from a different number of internal reflections in medium 2 (marked as colored arrows in Fig. 2.3) before the light eventually escapes. The same is true for the transmitted component. The total reflection can then be written as

$$r_{\mathrm{tot}}^{(\nu)} = r_{12}^{(\nu)} + t_{12}^{(\nu)}\Delta r_{23}^{(\nu)}\Delta t_{21}^{(\nu)} + t_{12}^{(\nu)}\Delta r_{23}^{(\nu)}\Delta r_{21}^{(\nu)}\Delta r_{23}^{(\nu)}\Delta t_{21}^{(\nu)} + ..., \tag{2.18}$$

where $\Delta = \exp(\mathrm{i}k_{z2}d)$ is a phase factor accounting for the extra distance traveled, and the coefficients $t_{ij}^{(\nu)}$ and $r_{ij}^{(\nu)}$ correspond to the ones from Eqs. (2.14) or Eqs. (2.16), for waves traveling from medium i to j. The color of each term in Eq. (2.18) corresponds to the matching lines in Fig. 2.3. Noticing the repeating behavior of Eq. (2.18), we can express it through a sum

$$r_{\mathrm{tot}}^{(\nu)} = r_{12}^{(\nu)} + t_{12}^{(\nu)}\Delta^2 r_{23}^{(\nu)} t_{21}^{(\nu)} \sum_{n=0}^{\infty}\left(\Delta^2 r_{21}^{(\nu)} r_{23}^{(\nu)}\right)^n, \tag{2.19}$$

which we recognize as the geometric series, and the total reflection becomes

$$r_{\mathrm{tot}}^{(\nu)} = r_{12}^{(\nu)} + \frac{t_{12}^{(\nu)}\Delta^2 r_{23}^{(\nu)} t_{21}^{(\nu)}}{1 - \Delta^2 r_{21}^{(\nu)} r_{23}^{(\nu)}}. \tag{2.20}$$

The singular behavior appearing when $\Delta^2 r_{21}^{(\nu)} r_{23}^{(\nu)} = 1$ represents the Fabry-Perot resonance that emerges due to the optical cavity [10].

For larger structures with an arbitrary number of layers, it becomes unmanageable to derive the Fresnel coefficients by explicitly accounting all possible light paths. Instead, in those cases we employ the transfer matrix method, which is discussed in Appendix. A. This technique enables us to easily extract the transmission and reflection coefficients from a single matrix, $\mathbf{M}^{\text{tot}} = \mathbf{M}^{\text{tot}}(\omega, k_{\parallel})$, given some N-layered structure. Furthermore, since the matrix is only 2×2, it is often very fast and efficient to compute.

2.2 Graphene Nanophotonics

Graphene is an atomically thin material, consisting of carbon atoms in a hexagonal pattern. It is of interest in the world of nanophotonics due to its remarkable electro-optical response, such as large charge carrier mobility, active tunability and high thermal conductivity. Furthermore, when doped, it can support highly confined surface-propagating modes known as surface plasmons. These unusual properties are due to the material's almost linear electronic dispersion near the Fermi level, as shown in Fig. 2.4(b), where the electrons can effectively be regarded as massless fermions with a velocity of $v_{\text{F}} \approx c/300$ [11]. This linear behavior also extends to its density of states, which is considerably smaller than that of traditional metal, meaning graphene needs significantly fewer dopant electrons to increase its Fermi energy compared to, e.g., gold or silver [12].

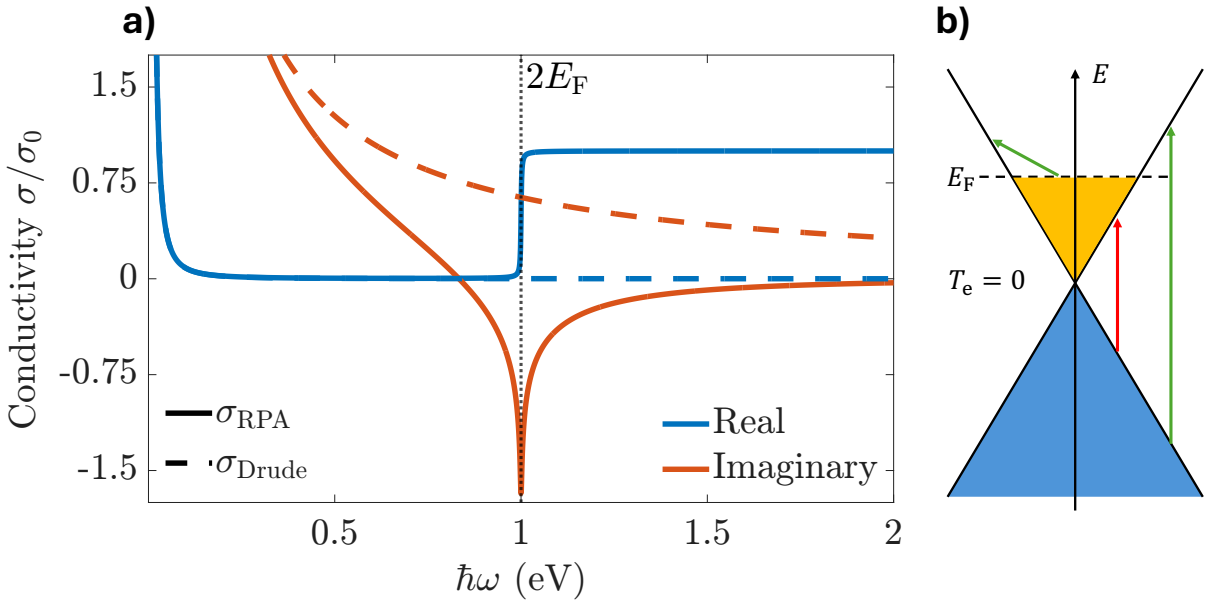

Figure 2.4: **(a)** A comparison between the local-Drude model and the local-RPA model normalized to $\sigma_0 = e^2/4\hbar$ for a Fermi level of $E_{\text{F}} = 0.5$ eV, a carrier mobility of $\mu_{\text{M}} = 10^4$ cm^2/V s and with $\gamma_{\text{Inter}} = \gamma_{\text{Intra}}$ using Eq. (2.22). **(b)** An illustration of the band structure of graphene, the blue area being the valence band and the yellow the conduction band. The green arrows show allowed transitions for electrons and red prohibited ones.

2.2.1 Optical Conductivity of Graphene

As discussed in Sec. 2.1.2, the inclusion of surface charges at an interface can be modeled by a conductivity. Thus, to incorporate a 2D material in a stratified structure, we only need its conductivity. In deriving Eqs. (2.14) and (2.16), we assumed a linear and isotropic response, and for graphene the conductivity is in general a function of frequency ω, in-plane wavevector $k_\parallel$, electron temperature T_e, chemical potential μ and damping rate γ. In this work, we will be assuming $T_\mathrm{e} = 0$, meaning the chemical potential (the energy it takes to add an electron to the system) is simply the Fermi energy, $\mu = E_\mathrm{F}$. Thus, when we refer to doped graphene, it means $E_\mathrm{F} > 0$, which in practice can be actively controlled through electro gating [13] or passively by chemical doping [14]. Since we will mostly be working in a low energy regime of $\hbar\omega < 0.1$ eV, this low temperature approximation works excellently [12].

When it comes to modeling the conductivity of graphene a selection of different models, of varying complexity, is available [15]. The simplest is the local Drude model (by local conductivity, we mean that its $k_\parallel$-dependence is ignored, and instead it is described by its value for $k_\parallel \approx 0$), which is given by

$$\sigma_\mathrm{Drude}(\omega) = \frac{\mathrm{i}e^2}{\pi\hbar^2}\frac{E_\mathrm{F}}{\omega + \mathrm{i}\gamma}, \tag{2.21}$$

where e is elementary charge, $\hbar$ is the reduced Planck constant, E_F is the Fermi energy and γ is a phenomenological damping parameter. The damping in graphene can be related to its carrier mobility (μ_M) through [16]

$$\gamma = \frac{ev_\mathrm{F}^2}{\mu_\mathrm{M} E_\mathrm{F}}. \tag{2.22}$$

Importantly, Eq. (2.21) only describes the conductivity contribution due to transitions within the conduction band of graphene, as depicted by the small oblique green arrow in Fig. 2.4(b). We can include the contribution of interband transitions (large vertical green arrow in the same figure) through the expression [17]

$$\sigma_\mathrm{Inter}(\omega) = \frac{\mathrm{i}e^2}{4\pi\hbar}\ln\left(\frac{2E_\mathrm{F} - \hbar\omega_\gamma}{2E_\mathrm{F} + \hbar\omega_\gamma}\right), \tag{2.23}$$

where $\omega_\gamma = \omega + \mathrm{i}\gamma_\mathrm{Inter}$ with γ_Inter being the damping associated with the interband. In the limit of $\gamma_\mathrm{Inter} \to 0$ the above expression can be written as

$$\sigma_\mathrm{Inter}(\omega) = \frac{e^2}{4\hbar}\left[\Theta(\hbar\omega - 2E_\mathrm{F}) + \frac{\mathrm{i}}{\pi}\ln\left|\frac{\hbar\omega - 2E_\mathrm{F}}{\hbar\omega + 2E_\mathrm{F}}\right|\right], \tag{2.24}$$

separating the real and imaginary parts explicitly. From the first term in this equation, it becomes clear how Pauli blocking prohibits valence electrons from absorbing energy and transitioning to the conduction band unless $\hbar\omega > 2E_\mathrm{F}$ (see red arrow in Fig. 2.4(b)). The inclusion of an interband damping smears the step function, as can be seen in Fig. 2.4(a), similarly to a non-zero temperature. This can be interpreted as collisions between the

electrons providing a small amount of additional energy, allowing for interband transitions even if $\hbar\omega \lesssim 2E_\mathrm{F}$.

Combining Eqs. (2.21) and (2.23) gives us

$$\sigma_\mathrm{RPA}(\omega, k_\parallel = 0) = \frac{\mathrm{i}e^2}{\pi\hbar^2}\frac{E_\mathrm{F}}{\omega + \mathrm{i}\gamma} + \frac{\mathrm{i}e^2}{4\pi\hbar}\ln\left(\frac{2E_\mathrm{F} - \hbar\omega_\gamma}{2E_\mathrm{F} + \hbar\omega_\gamma}\right), \tag{2.25}$$

which we will refer to as the local-RPA conductivity, since it can be obtained from using the random-phase approximation (RPA) and taking the local and low-temperature limit.

In cases where the local approximation is no longer appropriate, such as the case of highly confined plasmon modes where the in-plane momentum $k_\parallel$ becomes comparable to the Fermi momentum $k_\mathrm{F} = E_\mathrm{F}/\hbar v_\mathrm{F}$, the non-local RPA conductivity is instead used [18]

$$\sigma_\mathrm{RPA}(\omega, k_\parallel) = -\mathrm{i}\omega\chi(\omega, k_\parallel), \tag{2.26}$$

where

$$\chi(\omega, k_\parallel) = \frac{2e^2\omega}{\pi\hbar v_\mathrm{F}}\left\{\frac{k_\parallel}{k_\mathrm{F}} + \frac{[G(\Delta_-) - G(-\Delta_-) + \mathrm{i}\pi]\Theta(\mathrm{Re}\{\Delta_-\} + 1) + G(-\Delta_-) - G(\Delta_+)}{8\sqrt{\omega^2/v_\mathrm{F}^2 - k_\parallel^2}}\right\}, \tag{2.27}$$

is the electrical susceptibility at zero temperature. Furthermore, we have defined $G(z) = z\sqrt{z^2-1} - \ln\left(z + \sqrt{z^2-1}\right)$ and $\Delta_\pm = (\omega/v_\mathrm{F} \pm 2k_\mathrm{F})/k_\parallel$, with the square root taken in its principle branch (ensuring that the imaginary part is positive) and the imaginary part of the logarithm taken in the $[-\pi, \pi)$ sheet [11]. We will explore the differences between the local and non-local model more in depth in Sec. 2.3.1.

2.3 Surface-Plasmon Polaritons

Polaritons are quasiparticles created when light couples to a boson, such as an exciton, phonon or plasmon, in matter. Surface-plasmon polaritons (SPPs) are the coupling of plasma waves with light, traveling along a surface. Their dispersion relation in a given planar system is given by the poles of the Fresnel coefficient that describes that system, which can be interpreted as eigenmodes that are properties of the system and exist even if there are no external fields.

If no surface charges are present, and assuming non-magnetic materials, the poles of Eqs. (2.14) and (2.16) for a single interface between media 1 and 2 are

$$\frac{k_{z1}}{k_{z2}} = 0, \quad \text{s-polarized}, \tag{2.28a}$$

$$\frac{k_{z1}}{k_{z2}} + \frac{\varepsilon_1}{\varepsilon_2} = 0, \quad \text{p-polarized}, \tag{2.28b}$$

where only the p-polarized equation has a non-trivial solution. The dispersion relation is then

$$k_\parallel = \frac{\omega}{c}\sqrt{\frac{\varepsilon_{\mathrm{r},1}\varepsilon_{\mathrm{r},2}}{(\varepsilon_{\mathrm{r},1} + \varepsilon_{\mathrm{r},2})}}, \tag{2.29}$$

subject to the conditions $\mathrm{Re}\{\varepsilon_{\mathrm{r},1}\varepsilon_{\mathrm{r},2}\} < 0$ and $\mathrm{Re}\{\varepsilon_{\mathrm{r},1} + \varepsilon_{\mathrm{r},2}\} < 0$, meaning SPPs only exist at interfaces where there is a dielectric contrast (such as a dielectric-metal interface). Additionally, when considering lossy materials, the wavevector will have complex solutions, where the imaginary part is related to the propagation length, $L_{\mathrm{SPP}} = 1/2\mathrm{Im}\{k_\parallel\}$, which describes the distance traveled in plane by the plasmon before the intensity falls by 1/e. The real part is related to the plasmon wavelength through $\lambda_{\mathrm{SPP}} = 2\pi/\mathrm{Re}\{k_\parallel\}$, while the imaginary part of the out of plane wavevector, k_z, describes the penetration depth of the plasmon $\zeta = 1/\mathrm{Im}\{k_z\}$ [17]. If we instead chose to solve Eq. (2.29) for ω as a function of a real valued $k_\parallel$, we would end up with a complex frequency, $\omega = \omega' + \mathrm{i}\omega''$. In this case the imaginary part of the frequency would be related to the lifetime of the SPP since $\mathrm{e}^{-\mathrm{i}\omega t} \to \mathrm{e}^{-\mathrm{i}\omega' t}\mathrm{e}^{-\omega'' t}$. Nevertheless, the two pictures are equivalent.

To model the frequency-dependent permittivity of a metal, we can use the Drude model [19, 10]

$$\varepsilon_{\mathrm{r}}(\omega) = \varepsilon_{\mathrm{b}} - \frac{\omega_{\mathrm{p}}^2}{\omega(\omega + \mathrm{i}\gamma_{\mathrm{m}})}, \tag{2.30}$$

where $\omega_{\mathrm{p}} = \sqrt{ne^2/\varepsilon_0 m}$ is the plasma frequency, n is electron density, m is the electron effective mass and ε_{b} is the background permittivity. The parameters used in Eq. (2.30) are often acquired by fitting to experimental data.

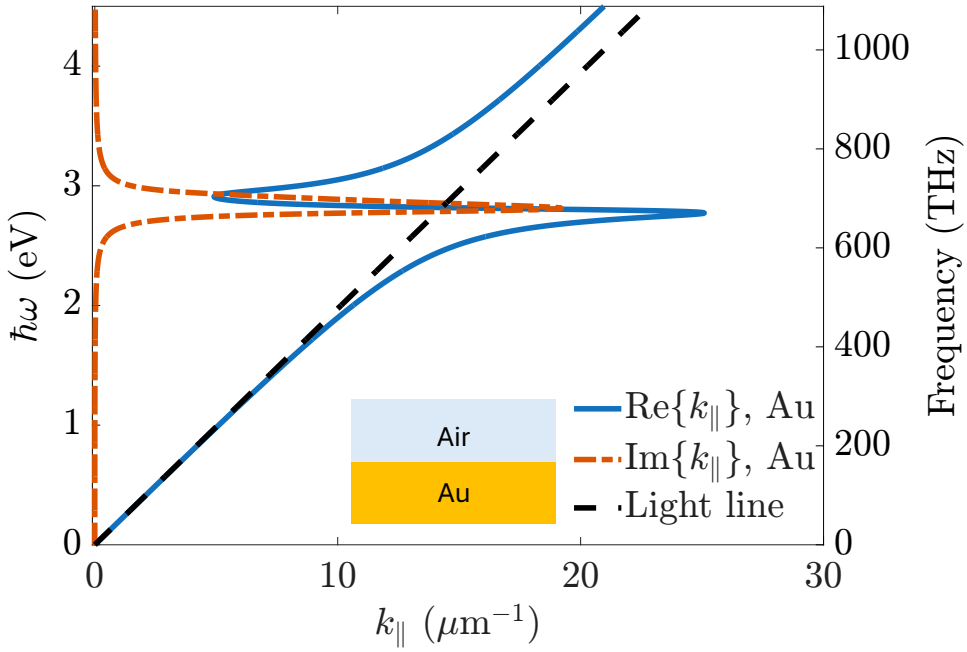

Figure 2.5: Real and imaginary parts of Eq. (2.29) for an air/gold interface (see inset), where the permittivity of gold was modeled using Eq. (2.30) with the parameters $\varepsilon_{\mathrm{b}} = 9.5$, $\hbar\omega_{\mathrm{p}} = 9.06$ eV and $\hbar\gamma_{\mathrm{m}} = 71$ meV [20]. The surface plasmon resonance is $\hbar\omega_{\mathrm{sp}} \approx 2.8$ eV.

Figure 2.5 shows a dispersion relation calculated using Eq. (2.29) for an air/gold interface, where the permittivity of gold was calculated with Eq. (2.30), with parameters taken from Ref. 20 (see also caption). At low frequencies, the plasmon wavevector is

indistinguishable from the light line, but as we go to higher energies, it starts to diverge from the light line into larger wavevector values. The wavevector is maximized at the *surface plasmon frequency*, which is given by the pole of Eq. (2.29)

$$\omega_{\mathrm{sp}} = \frac{\omega_{\mathrm{p}}}{\sqrt{\varepsilon_{\mathrm{b}} + \varepsilon_{\mathrm{r},1}}}, \tag{2.31}$$

assuming $\gamma_{\mathrm{m}} = 0$. At this point, the plasmon is highly confined to the surface and reaches the smallest allowed wavelength. However, around ω_{sp} the imaginary part of $k_{\parallel}$ also increases, lowering the propagation length, meaning a high level of confinement comes at a cost of shorter propagation length. Additionally, as the frequency reaches values slightly larger than the surface plasmon frequency, $\mathrm{Im}\{k_{\parallel}\}$ increases rapidly such that the plasmon becomes overdamped. Here, the real part of the wavevector crosses back into the light cone, and there is no longer plasmon activity.

The high level of confinement $\lambda/\lambda_{\mathrm{SPP}}$ of SPPs (compared to the free-space photon wavelength $\lambda = 2\pi c/\omega$) is one of their key appeals, since this allows one to probe with light below the diffraction limit. However, since plasmons are characterized by existing outside the light cone, it becomes a challenge to excite them. At no point, except at the backbend, does the light line cross the SPP dispersion, and therefore there is a mismatch in momentum between a photon and an SPP, impeding the direct excitation of SPPs with light. This issue can be solved by a number of different methods, such as the use of evanescent light from a prism, dipole/tip scattering or free-electron beams [21]. In this work, we model a probing tip as a point dipole, which mathematically is represented as a Dirac-delta function in space. The extreme localization in space must, in turn, result in a broad spectrum of the momentum, due to the uncertainty principle, allowing the field radiated by the dipole to couple to the SPPs of a nearby surface. This is realized in the near-field of the dipole in terms of evanescent waves, which can then excite plasmons at the interface.

2.3.1 Graphene Plasmons

Having introduced the fundamentals of traditional SPPs in dielectic-metal interfaces, we now turn our attention to graphene surface-plasmon polaritons (GSPPs). We found in Sec. 2.1.2 that, to describe the response of a 2D material, we can simply include its optical conductivity in the Fresnel coefficients. Again, we look at the pole of the p-polarized Fresnel coefficients[1]

$$k_{z1}\varepsilon_2 + k_{z2}\varepsilon_1 + k_{z1}k_{z2}\frac{\sigma}{\omega} = 0, \tag{2.32}$$

where k_{zi} and σ are functions of frequency and wavevector, and the permittivities may also be functions of frequency. Even when using the simple Drude model for conductivity, Eq. (2.21), the above equation has no analytical solutions, but can readily be solved numerically, as shown in Fig. 2.6. Importantly, contrary to the traditional plasmons, we

[1] In principle, it is possible to have s-polarized plasmons in graphene. However, they are poorly confined compared to p modes, making them less appealing and will therefore not be examined closely [17].

are no longer restricted to dielectric-metal interfaces, i.e., a dielectric-graphene-dielectric "sandwich" can support plasmons, since doped graphene can behave approximately like a metal.

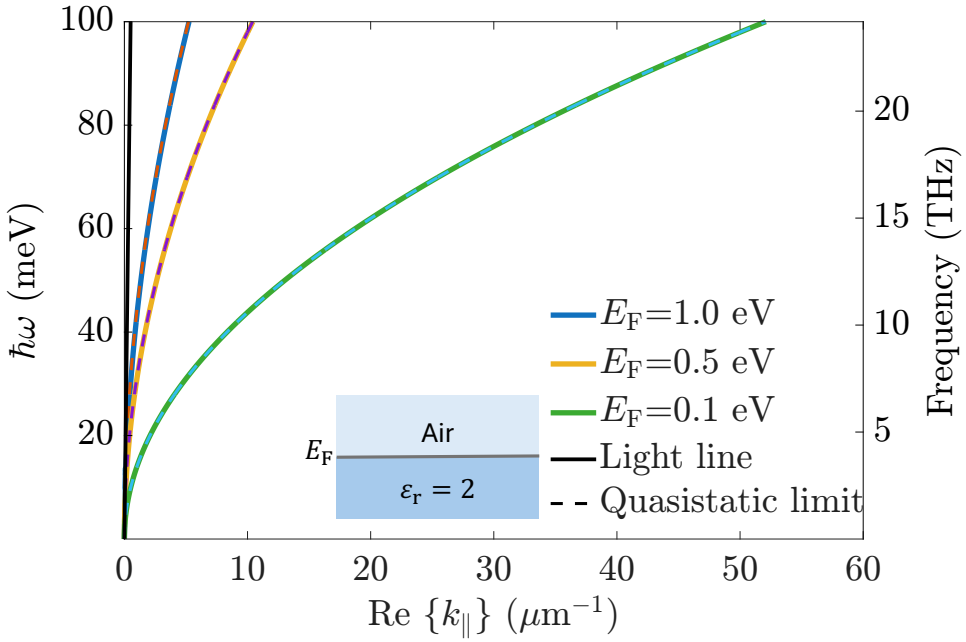

Figure 2.6: Solution of Eq. (2.32) for three different graphene doping levels (see legend), using the local Drude model for the conductivity. The graphene sheet is placed between two dielectrics, $\varepsilon_{r,1} = 1$ and $\varepsilon_{r,2} = 2$, and we use a carrier mobility of $\mu_M = 10^3$ cm^2/Vs. The dotted lines lying on top of of the solid lines are their respective quasistatic limit approximations, given by Eq. (2.33).

In Fig. 2.6 we show the dispersion relation for a graphene sheet doped with three different values (see legend). Compared to the gold plasmons, GSPPs are more confined and are excited at lower energies. Additionally, while gold plasmons have a wavelength limit (below which gold stops behaving like a metal), this is not the case for graphene, where we see no backbend. However, the momentum-mismatch issue when exciting the plasmons remains, as the light line does not cross the plasmon dispersion, and we therefore still need some other means of exciting them.

Another feature of the GSPPs is their dependence on the doping of the graphene, which, as mentioned earlier, can be actively tuned. An approximate dependence on the doping can be found by taking the quasistatic limit of Eq. (2.32) ($c \to \infty$, $k_{zj} \to \mathrm{i}k_\parallel$) and using the local Drude model for the conductivity, Eq (2.21). This allows for an analytical expression for the GSPP dispersion

$$\omega = \sqrt{\frac{e^2 E_F}{\pi\hbar^2(\varepsilon_1 + \varepsilon_2)}}k_\parallel, \tag{2.33}$$

where we have assumed negligible damping. We see that the energy has a square root dependence on the both the Fermi energy and the wavevector. As we can see from the Fig. 2.6, this approximation holds very well in the THz regime.

When considering the case of multiple parallel graphene sheets (or, e.g., a graphene sheet in the vicinity of a metallic surface), we can derive the corresponding SPP dispersion in the same way: we compute the Fresnel coefficient $r(\omega, k_\parallel)$ of the combined structure and find its complex poles through the equation $1/r(\omega, k_\parallel) = 0$. However, it is often more convenient to introduce an alternative way to theoretically probe plasmons, called the *loss function* [22]

$$L(\omega, k_\parallel) = \mathrm{Im}\{r\}. \tag{2.34}$$

When plasmons are excited, the energy they absorb is captured in the imaginary part of reflection coefficient of the system, and it therefore acts as a measure of plasmon activity. Interestingly, an additional feature of the loss function, not directly indicated by the dispersion curve, is the "intensity" of the plasmon (i.e., roughly a measure of how strong its associated near fields are), which is affected by the doping and quality (damping) of the graphene.

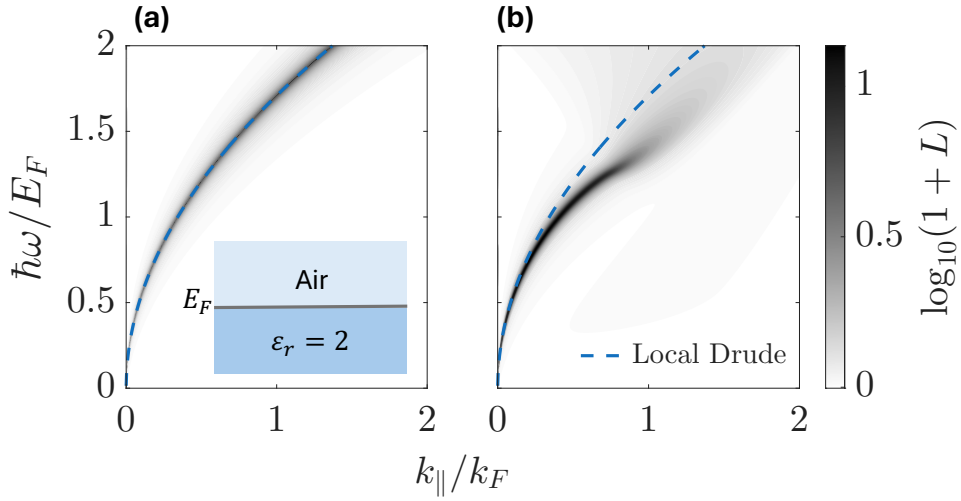

Figure 2.7: Loss function L of a dielectric-graphene-dielectric system, where the dashed line is the numerically-solved dispersion relation, as a function of in-plane wavevector (normalized to the Fermi wavevector $k_\mathrm{F} = E_\mathrm{F}/\hbar v_\mathrm{F}$) and frequency (normalized to the Fermi energy), describing the graphene conductivity using **(a)** the local Drude model and **(b)** the non-local RPA conductivity. In both cases, we used $E_\mathrm{F} = 0.5$ eV and $\mu_\mathrm{M} = 10^3$ cm^2/Vs.

Figure 2.7(a) shows the loss function compared to the numerical dispersion given by solving Eq. (2.32) with the local Drude model in Eq. (2.21), exhibiting an excellent agreement. In contrast, in Fig. 2.7(b), we describe the same system, but using the non-local RPA conductivity in Eq. (2.26). The local result is in good agreement with the loss function for lower energies, but around $\hbar\omega = E_\mathrm{F}$ and $k_\parallel = k_\mathrm{F}$ there is enough energy and momentum that electrons in the valence band can be promoted to the conduction band, meaning less energy goes to the excitation of plasmons.

In practice, we often deal with more complex structures than single interfaces. Luckily, using the transfer matrix formalism discussed in the Appendix A, we can readily model

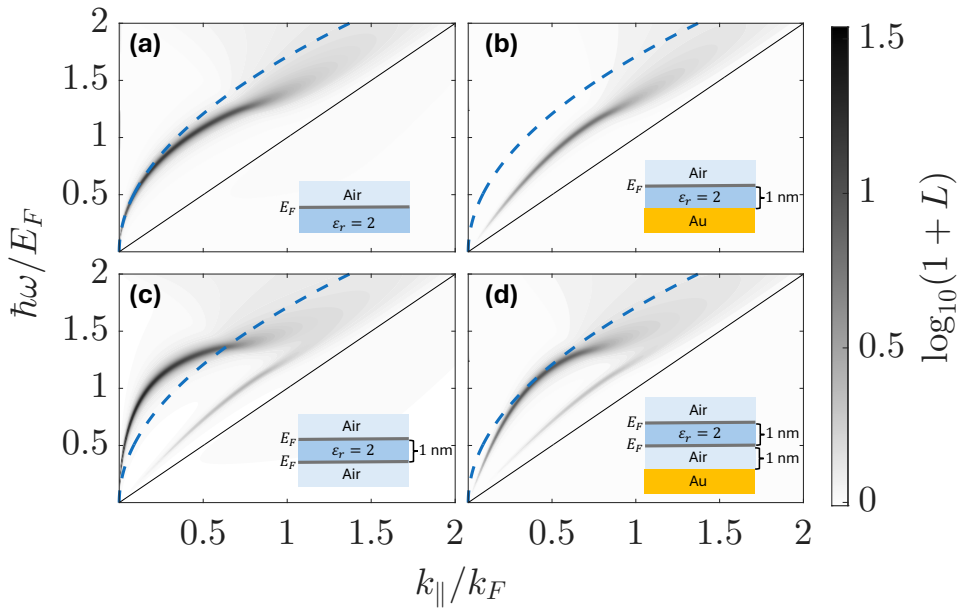

Figure 2.8: Loss function for various layered structures (see insets), using $E_\mathrm{F} = 0.5$ eV, $\mu_\mathrm{M} = 10^3$ cm^2/Vs and using the non-local RPA conductivity, with the dotted line being the local Drude model in the quasistatic limit, Eq. (2.33). Additionally, the diagonal line shows the Fermi velocity of graphene electrons, $v_\mathrm{F} = E_\mathrm{F}/\hbar k_\mathrm{F}$. To model the gold, we use the same model as in Fig. 2.5. The inset in each plot shows the corresponding system. **(a)** A simple single interface system, the same as in Fig. 2.7, used for reference. **(b)** The second dielectric now has a thickness of $d = 1$ nm followed by gold. **(c)** The third layer is now air instead and we add an additional equivalent graphene sheet at the second interface. **(d)** We add a gold layer to the bottom of the former system, and the third layer now has a thickness of $d = 1$ nm.

multilayered systems with multiple graphene sheets! In Fig. 2.8, we compare four different systems via their corresponding loss function: a single graphene sheet, a double graphene sheet, a graphene sheet on gold, and a double graphene sheet on gold.

Figure 2.8(a) is equivalent to Fig. 2.7(b). In Fig. 2.8(c), we add an additional graphene sheet $d = 1$ nm below the first and, compared to Fig. 2.8(a), this causes a splitting in the dispersion. This is due to the two sheets hybridizing, allowing for two plasmon modes, instead of one. The upper branch is called the optical mode, where the charges at each interface oscillates in phase, and the E_z component is anti-symmetric with respect to $z = d/2$. The lower branch is the acoustic mode and, here, the out of plane electric field component is symmetric, and the charge oscillations are in anti-phase [17]. The splitting of the dispersion is directly tied to the separation of the layers, d, since, as discussed earlier, the field of the plasmons decays exponentially out of plane. This is why the two modes start to converge to a single mode at higher energy/momentum; here the penetration depth of the plasmon is too small to reach the second sheet, and we recover the single sheet solution.

In Fig. 2.8(b), we only have a single sheet of graphene, but the third material is now gold, which, in this energy range, acts like a perfect mirror. The oscillations of the

electrons in the graphene are mirrored in the gold, creating what is called *image plasmon polaritons* [23], which act in a similar way to a second graphene sheet. However, since the gold mirrors the graphene plasmons, the anti-symmetric modes cancel, leaving only the symmetric acoustic mode. The result is a single mode that is more confined compared to the isolated graphene sheet in Fig. 2.8(a). Comparing Fig. 2.8(c) and (d), we see that the addition of a gold layer at the bottom again "pushes" the dispersion further down, allowing for larger confinement.

Finally, in each plot in Fig. 2.8, we also show the Fermi velocity $v_{\mathrm{F}} = E_{\mathrm{F}}/\hbar k_{\mathrm{F}}$ as a solid diagonal line, which roughly represents an upper limit to the maximum level of confinement. Below this line, the group velocity of the light, $v_{\mathrm{g}} = \partial\omega/\partial k_{\parallel}$, is too slow compared to the velocity of the electrons, v_{F}, meaning they can not couple properly.

Graphene Ribbons

This work has so far focused on extended surfaces, which has the disadvantage that they rely on external elements like tips/point dipoles to excite plasmons. Alternatively, finite graphene structures, such as a ribbon, allow for the direct excitation of plasmons without the use of a dipole due to their lack of translational invariance. In what follows, we make a superficial presentation of the methods used to model graphene ribbons, while a more detailed presentation can be found in Refs. 24, 25. For simplicity, we only consider free-standing graphene ribbons, i.e. without a substrate supporting them.

In contrast with the graphene sheet, the ribbon has a semi-analytical closed form dispersion relation, when using the local Drude model in Eq. (2.21) to describe its conductivity. It can be shown that, for the ribbon, the plasmonic modes obey the relation

$$\eta(k_y, W) = \frac{\mathrm{i}\sigma(\omega)}{4\pi\varepsilon_0\omega W}, \tag{2.35}$$

where W is the width of the ribbon, k_y is the wavevector along the length of the ribbon and $\eta(k_y, W)$ is a geometric parameter found by solving an eigenvalue problem (see Ref. 24). Another difference between the extended graphene and the ribbon is that the ribbon supports multiple modes (in a similar way that the infinite square well, from quantum mechanics, has multiple energy modes characterized by a quantum number n). In Fig. 2.9 we show the first four modes of a doped graphene ribbon. As mentioned, it is clear that we can excite plasmons directly with light, since the light line crosses the plasmon modes.

A general property of graphene ribbons is that their dispersion lowers with the increasing of their width, because the standing plasmon waves must have an increased wavelength to compensate. The inverse is true for the Fermi energy, allowing for both passive and active tunability in the THz frequency range. This can be seen in Fig. 2.10, where we have calculated the extinction cross section of graphene ribbons of varying size and Fermi energies, being illuminated by an external spatially uniform electric field, using

$$\sigma^{\mathrm{ext}} = \frac{\omega}{\varepsilon_0 c\sqrt{\varepsilon_r}}\mathrm{Im}\{\alpha(\omega)\}, \tag{2.36}$$

where α is the polarizability of the ribbon. Since graphene is atomically thin, it scatters little light and the extinction is effectively a measure of light absorbed, i.e. the excitation

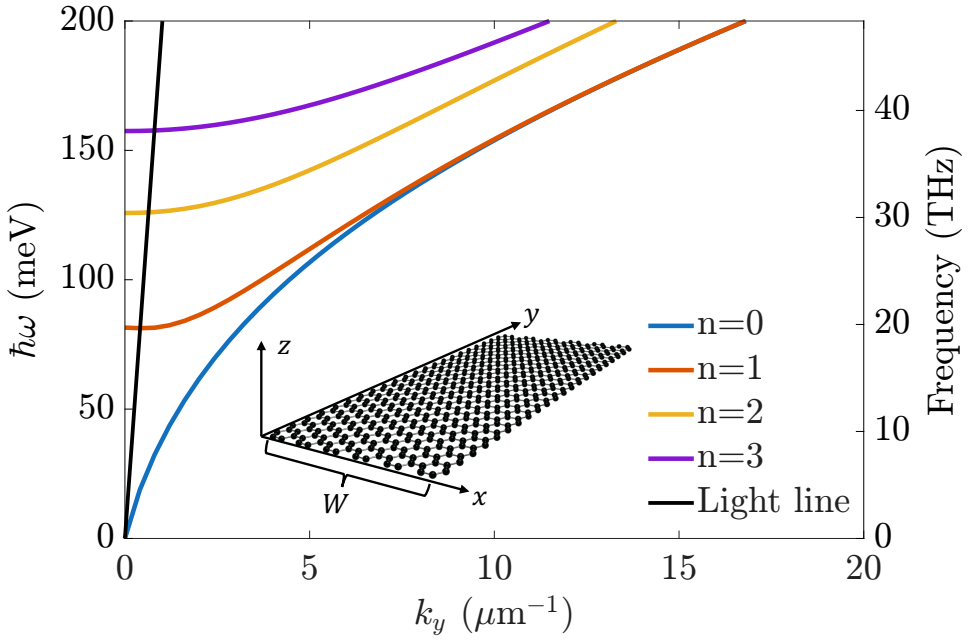

Figure 2.9: Dispersion relation of graphene ribbon, using the local Drude conductivity and a carrier mobility of $\mu_{\mathrm{M}} = 10^3$ cm^2/Vs, a doping of $E_{\mathrm{F}} = 1$ eV and ribbon width of $W = 1$ μm.

of plasmons. We can clearly identify the $n = 1$ modes from the different structures in Fig. 2.9 as resonances in the extinction, at around $\hbar\omega \approx 80$ meV. The second set of peaks we see, around $\omega \approx 34$, are the $n = 3$ modes. The $n = 2$ modes do not appear, since even modes cannot be excited by a direct incident light, as we have used here. An additional characteristic of the graphene plasmons is that the extinction per area is around 3.5 for the two highly doped ribbons, meaning they "funnel in" light that would have "missed" the ribbon.

Finally, we address how to incorporate graphene ribbons into the Green's function formalism that is presented in the following section. From Fig. 2.10, it is clear that the first mode of the ribbon is dominant, since the second mode is unable to be excited and third is very weak. As such, we can model the ribbon using only its $n = 1$ mode, and its response to an external uniform field can be written as [26]

$$\alpha_1 = 4\pi\varepsilon_0 W^2 \frac{\zeta_1^2}{1/\eta(\omega) - 1/\eta_1}, \tag{2.37}$$

where $\zeta_1 = 0.942$, $\eta_1 = -0.069$ and $\eta(\omega)$ is given by Eq. (2.35). In Sec. 2.4.2 we show how the electric field of a dipole is related to its dipole moment, when placed near a photonic environment. To incorporate a ribbon, we would simply approximate it as a point dipole, characterized by the polarizability given in Eq. (2.37). This is of course a rough approximation, especially if the ribbon is placed close to an interface, so the results should be regarded as initial estimates rather than exact results.

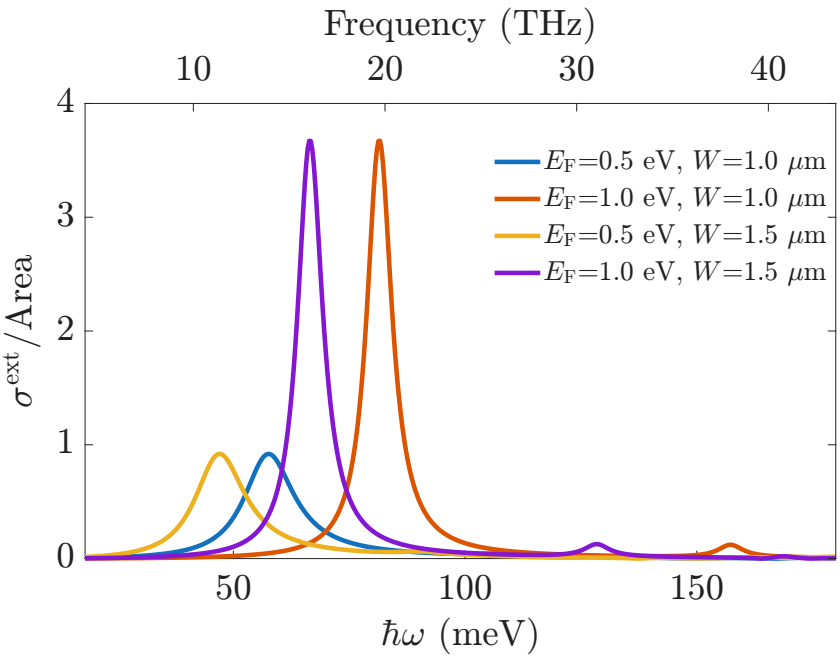

Figure 2.10: The extinction cross section for graphene ribbons of varying size and doping. We used the local Drude conductivity model and a carrier mobility of $\mu_{\text{M}} = 10^3$ cm^2/Vs.

2.4 Green's Functions

Having established a framework to examine different stratified structures, we are now left with the task of calculating the related fields that arise from probing said structures. This can be done using the Green's function formalism. An in-depth review of Green's functions can be found in many textbooks (e.g., Ref. 10), but, for our purposes, we can simply think of the Green's function $\mathbf{G}(\mathbf{r}, \mathbf{r}')$ as a function that, given some source at $\mathbf{r}_0$ in a given system, returns the electric field at $\mathbf{r}$. More specifically, for time-harmonic fields of frequency ω, the electric field, given some current density $\mathbf{j}$, is

$$\mathbf{E}_\omega(\mathbf{r}) = \mathrm{i}\omega\mu \int \mathrm{d}^3\mathbf{r}'\mathbf{G}(\mathbf{r}, \mathbf{r}') \cdot \mathbf{j}(\mathbf{r}'), \tag{2.38}$$

where it should be understood that $\mathbf{G}$ is a 3×3 matrix, sometimes referred to as the Green's tensor. Notably, the free-space Green's function for a point source in a uniform medium is given by

$$G_{ij}(\mathbf{r}, \mathbf{r}_0) = \left(\delta_{ij} + \frac{\partial_i \partial_j}{k_0^2}\right) \frac{\mathrm{e}^{\mathrm{i}k_0|\mathbf{r}-\mathbf{r}_0|}}{4\pi|\mathbf{r} - \mathbf{r}_0|}, \tag{2.39}$$

where i, j denote the tensor components, δ_{ij} is the identity matrix and $k_0 = \omega/c$ is the free space wavevector.

In what follows, we extend this formalism to arbitrary layered structures with translational invariance whose optical properties are obtained through the transfer matrix method described in Appendix A, allowing us to acquire the Green's function for an arbitrarily large stratified structure, as illustrated in Fig. 2.11.

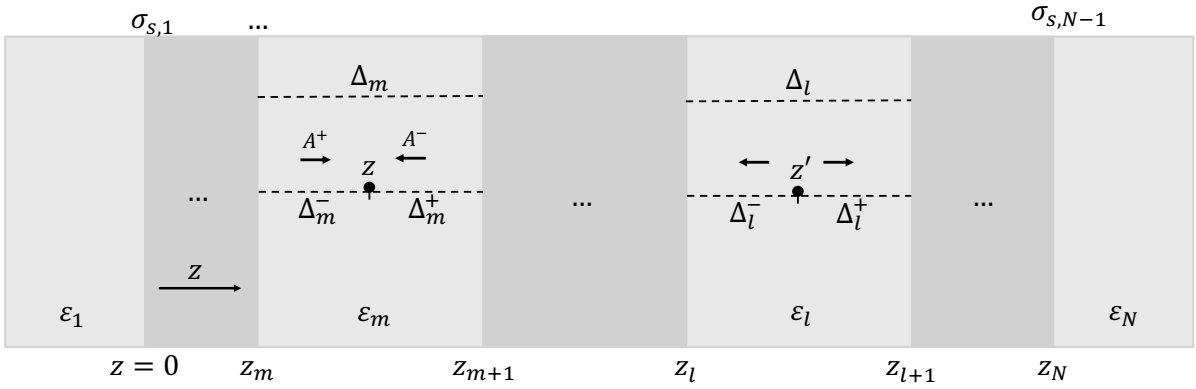

Figure 2.11: Illustration of the a N-layered structure with potentially N different materials and $N-1$ different interface conductivities. In this example, the source is located in layer l, which is located above the observation point at layer m, emitting in both the positive and negative z-direction.

2.4.1 Green's Function for Stratified Media

We assume that the materials extend infinitely in the xy-plane and only vary in the z direction. In this case, it can be shown that, for an unbounded medium, the Green's function is given by [10]

$$G_{ij}(\mathbf{r},\mathbf{r}') = -\frac{\hat{z}_i\hat{z}_j}{k^2}\delta(\mathbf{r}-\mathbf{r}') + \frac{\mathrm{i}}{8\pi^2}\sum_{\nu=\mathrm{s,p}}\int \mathrm{d}^2\mathbf{k}_\parallel \frac{\mathrm{e}^{\mathrm{i}\mathbf{k}_\parallel\cdot\mathbf{R}}}{k_z}\hat{\varepsilon}_i^{(\nu)}(\hat{\mathbf{k}}^\pm)\hat{\varepsilon}_j^{(\nu)}(\hat{\mathbf{k}}^\pm), \tag{2.40}$$

where $\mathbf{R} = (x-x')\hat{\mathbf{x}} + (y-y')\hat{\mathbf{y}}$, $\mathbf{k}_\parallel = k_x\hat{\mathbf{x}} + k_y\hat{\mathbf{y}}$ and $\hat{\varepsilon}_i^{(\nu)}$ is the polarizability vector given by

$$\hat{\varepsilon}^{(\mathrm{s})} = \frac{1}{k_\parallel}(k_y\hat{\mathbf{x}} - k_x\hat{\mathbf{y}}) \tag{2.41a}$$

$$\hat{\varepsilon}^{(\pm,\mathrm{p})} = \pm\frac{k_z}{kk_\parallel}(k_x\hat{\mathbf{x}} + k_y\hat{\mathbf{y}}) - \frac{k_\parallel}{k}\hat{\mathbf{z}}, \tag{2.41b}$$

where $k = \sqrt{k_x^2+k_y^2+k_z^2}$, $k_\parallel = \sqrt{k_x^2+k_y^2}$ and the $\pm$ sign is chosen depending on the direction of propagation (i.e. $+$ for fields propagating in the positive z direction and vice versa for $-$).

The Green's function in Eq. (2.40) does not account for possible boundaries, but this can be remedied by introducing *amplitude coefficients*, A, which are scalars consisting of a "mix" of transmission and reflection coefficients that ensure proper continuity of the fields. The more general Green's function, describing the field in medium m when the source is located in medium l, then takes the form

$$\begin{aligned} G_{ij}(\mathbf{r},\mathbf{r}') = &-\frac{\hat{z}_i\hat{z}_j}{k_l^2}\delta(\mathbf{r}-\mathbf{r}') \\ &+ \frac{\mathrm{i}}{8\pi^2}\sum_{\nu=\mathrm{s,p}}\sum_{\substack{\sigma_1=\pm\\ \sigma_2=\pm}}\int \mathrm{d}^2\mathbf{k}_\parallel \frac{\mathrm{e}^{\mathrm{i}\mathbf{R}\cdot\mathbf{k}_\parallel}}{k_{lz}}A_{lm}^{(\sigma_1,\sigma_2,\nu)}(k_\parallel,z,z')\hat{\varepsilon}_i^{(\nu)}(\hat{\mathbf{k}}_m^{(\sigma_2)})\hat{\varepsilon}_j^{(\nu)}(\hat{\mathbf{k}}_l^{(\sigma_1)}). \end{aligned} \tag{2.42}$$

Let us carefully examine the second term. First, just as with the Fresnel coefficients, we have split the equation into s-polarized and p-polarized fields, and the first sum picks up both contributions. Secondly, as the source (z') might be located above ($z' > z$) or below ($z' < z$) the observation point (z), we must account for the direction of the field as it is emitted ($\sigma_1 = \pm$) and direction of the field as it is "observed" ($\sigma_2 = \pm$). The second and third sum over σ_1 and σ_2 ensure we account for all possible combinations. Next, we have introduced the aforementioned amplitude coefficient $A_{lm}^{(\sigma_1,\sigma_2,\nu)}(k_\parallel, z, z')$, which is dependent on both emission and "observation" direction, the polarizability of the field, the in-plane wavevector and the location of observation and the source. The z and z' dependence could in principle be extracted from A, simplifying it, but we found it to be both more "pedagogical" and computationally robust to leave it as above. Finally, we have the two polarizability vectors, whose role is more clear now: $\hat{\varepsilon}_i$ accounts for the polarizability of the field as it is observed in material m, while $\hat{\varepsilon}_j$ accounts for the polarizability of the field as it is emitted in layer l. In this way, they also contribute to the tensor structure of the Green's function: $E_i \propto G_{ij} j_j$, i.e. the first index is connected to field while the second is connected to the source.

Empirical Derivation of Amplitude Coefficients

The amplitude coefficients, ensuring the continuity of the Green's function, can be grouped into three cases: when $l > m$, $l < m$ and $l = m$. We will consider the first one and the other cases follow in a similar manner. The system we want to determine the amplitude coefficients for is depicted in Fig. 2.11, where some source located in layer l at position z' emits a field that we then want to know in layer m at position z. In the illustration we have defined three kinds of phases that we use to propagate the fields

$$\Delta_i = \mathrm{e}^{\mathrm{i}k_{zi}(z_{i+1}-z_i)}, \tag{2.43a}$$

$$\Delta_i^+ = \mathrm{e}^{\mathrm{i}k_{zi}(z_{i+1}-\tilde{z}_i)}, \tag{2.43b}$$

$$\Delta_i^- = \mathrm{e}^{-\mathrm{i}k_{zi}(z_i-\tilde{z}_i)}, \tag{2.43c}$$

where $i = l, m$ and correspondingly $\tilde{z}_i = (z', z)$. Combining the phases with the appropriate transmission and reflection coefficients, we can generate the necessary amplitude coefficients. One thing in common with almost all the coefficients is that they must be proportional to the effective transmission coefficient $\tilde{t}_{lm}^{(\nu)}$ from layer l into layer m. Additionally, we must account for the Fabry-Perot resonance that occurs due to the multiple reflections in the source layer and the observation layer (that are not accounted for in $\tilde{t}_{lm}^{(\nu)}$). This common behavior is captured in the quantity

$$\Lambda^{(\nu)} = \frac{\tilde{t}_{lm}^{(\nu)}}{(1 - \Delta_l^2 \tilde{r}_{l1}^{(\nu)} \tilde{r}_{lN}^{(\nu)})(1 - \Delta_m^2 \tilde{r}_{m1}^{(\nu)} \tilde{r}_{ml}^{(\nu)})}, \tag{2.44}$$

where $\tilde{r}_{ij}$ is the effective reflection coefficient connecting medium i and medium j, which, along with $\tilde{t}_{ij}$, can be obtained using the transfer matrix formalism for a structure spanning layers i to j. It is important to note that, when calculating the Fresnel coefficients, we must keep track of the direction of propagation. For the system above, the transmission coefficient would always be the "backwards" one, i.e., Eq. (A.24) rather than

Eq. (A.18a), and similarly for the reflection coefficients. Finally, we note that the two parentheses in the denominator of Eq. (2.44) represent the Fabry-Perot resonances on the source layer and the observation layer. However, they are not "symmetric" in the sense that the source layer reflection coefficients spans the entire structure, i.e. the first one goes from layer l to 1 and the second one from l to N, while, for the observation layer, the first one goes from m to 1 but the second one goes from m to l. This is to avoid double counting, which is less obvious from an empirical point of view.

As an example of an amplitude coefficient, we will consider a field being emitted upwards and observed going downwards, $A_{lm}^{(+,-)}$. As mentioned above, we first include the global $\Lambda^{(\nu)}$. Next, we gain a Δ_l^+ phase from traveling towards the upper interface of the l-layer before reflecting, which contributes a factor $\tilde{r}_{l,N}^{(\nu)}$. Finally, we need to propagate the wave all the way to the lower boundary of layer l, Δ_l, and to the observation point, Δ_m^+. Combining these contributions, we get

$$A_{lm}^{(+,-,\nu)} = \Lambda^{(\nu)} \Delta_l^+ \tilde{r}_{lN}^{(\nu)} \Delta_l \Delta_m^+. \tag{2.45a}$$

Following this procedure we determine the other three combinations, giving us

$$A_{lm}^{(+,+,\nu)} = \Lambda^{(\nu)} \Delta_l^+ \tilde{r}_{lN}^{(\nu)} \Delta_l \Delta_m \tilde{r}_{m1}^{(\nu)} \Delta_m^-, \tag{2.45b}$$

$$A_{lm}^{(-,+,\nu)} = \Lambda^{(\nu)} \Delta_l^- \Delta_m \tilde{r}_{m1}^{(\nu)} \Delta_m^-, \tag{2.45c}$$

$$A_{lm}^{(-,-,\nu)} = \Lambda^{(\nu)} \Delta_l^- \Delta_m^+. \tag{2.45d}$$

The coefficients for the $l < m$ case follow in a very similar manner, as can be seen in Table 2.1, but they differ slightly in the case when source and observation are in the same layer. Here, we no longer have two cavity resonances or a transmission coefficient. Furthermore, for the $(+,+)$ and $(-,-)$ cases we need to account for the direct field of the source, which is done by introducing the Heaviside step function $\Theta(x)$, that in this case takes a value of one when $x > 0$ and zero otherwise.

	$l > m$	$l < m$	$l = m$
$A_{lm}^{(+,-,\nu)}$	$\Lambda^{(\nu)} \Delta_l^+ \tilde{r}_{lN}^{(\nu)} \Delta_l \Delta_m^+$	$\Lambda^{(\nu)} \Delta_l^+ \Delta_m \tilde{r}_{mN}^{(\nu)} \Delta_m^+$	$\frac{\Delta_l^+ \tilde{r}_{mN}^{(\nu)} \Delta_m^+}{1 - \tilde{r}_{mN}^{(\nu)} \tilde{r}_{mN}^{(\nu)} \Delta_m^2}$
$A_{lm}^{(+,+,\nu)}$	$\Lambda^{(\nu)} \Delta_l^+ \tilde{r}_{lN}^{(\nu)} \Delta_l \Delta_m \tilde{r}_{m1} \Delta_m^-$	$\Lambda^{(\nu)} \Delta_l^+ \Delta_m^-$	$\Delta_z^+ \Theta^+ + \frac{\Delta_l^+ \tilde{r}_{mN}^{(\nu)} \Delta_m \tilde{r}_{m1}^{(\nu)} \Delta_m^-}{1 - \tilde{r}_{mN}^{(\nu)} \tilde{r}_{mN}^{(\nu)} \Delta_m^2}$
$A_{lm}^{(-,+,\nu)}$	$\Lambda^{(\nu)} \Delta_l^- \Delta_m \tilde{r}_{m1}^{(\nu)} \Delta_m^-$	$\Lambda^{(\nu)} \Delta_l^- \tilde{r}_{l1}^{(\nu)} \Delta_l \Delta_m^-$	$\frac{\Delta_l^- \tilde{r}_{m1}^{(\nu)} \Delta_m^-}{1 - \tilde{r}_{mN}^{(\nu)} \tilde{r}_{mN}^{(\nu)} \Delta_m^2}$
$A_{lm}^{(-,-,\nu)}$	$\Lambda^{(\nu)} \Delta_l^- \Delta_m^+$	$\Lambda^{(\nu)} \Delta_l^- \tilde{r}_{l1}^{(\nu)} \Delta_l \Delta_m \tilde{r}_{mN}^{(\nu)} \Delta_m^+$	$\Delta_z^- \Theta^- + \frac{\Delta_l^- \tilde{r}_{m1}^{(\nu)} \Delta_m \tilde{r}_{mN}^{(\nu)} \Delta_m^+}{1 - \tilde{r}_{mN}^{(\nu)} \tilde{r}_{mN}^{(\nu)} \Delta_m^2}$

Table 2.1: Amplitude coefficients used to calculate the Green's function for stratified media, expressed in terms of propagation phases in Eq. (2.43) and generalized reflection and transmission coefficients. Additionally, we have defined $\Theta^{\pm} \equiv \Theta[\pm(z - z')]$ accounting for the direct field and $\Delta_z^{\pm} \equiv \mathrm{e}^{\pm \mathrm{i} k_{zm}(z - z')}$, which accounts for the phase of the direct field.

Since we work with extended surfaces, the Fresnel coefficients only depend on the magnitude of the wavevector $k_{\parallel} = \sqrt{k_x^2 + k_y^2}$, so we can go to polar coordinates

$$\int \mathrm{d}^2 \mathbf{k}_{\parallel} \to \int_0^{\infty} \mathrm{d}k_{\parallel} \; k_{\parallel} \int_0^{2\pi} \mathrm{d}\varphi_{\mathbf{k}_{\parallel}}, \tag{2.46}$$

and use Table 2.2 to perform the angular integral. Equation. (2.42) now takes the form

$$G_{ij}(\mathbf{r},\mathbf{r}') = -\frac{\hat{z}_i\hat{z}_j}{k_l^2}\delta(\mathbf{r}-\mathbf{r}') + \frac{\mathrm{i}}{4\pi}\sum_{\nu=\mathrm{s,p}}\sum_{\substack{\sigma_1=\pm\\ \sigma_2=\pm}}\int \mathrm{d}k_\parallel \frac{k_\parallel}{k_{lz}} A_{lm}^{(\sigma_1,\sigma_2,\nu)}(k_\parallel,z,z')\left\langle \hat{\varepsilon}_i^{(\nu)}(\hat{\mathbf{k}}_m^{(\sigma_2)})\hat{\varepsilon}_j^{(\nu)}(\hat{\mathbf{k}}_l^{(\sigma_1)})\right\rangle, \quad (2.47)$$

having defined, for s-polarization,

$$\left\langle \hat{\varepsilon}^{(\mathrm{s})}(\hat{\mathbf{k}}_m^{(\sigma_2)})\hat{\varepsilon}^{(\mathrm{s})}(\hat{\mathbf{k}}_l^{(\sigma_1)})\right\rangle = \frac{1}{2}\begin{pmatrix} \mathcal{J}^+ & \sin(2\varphi)J_2 & 0\\ \sin(2\varphi)J_2 & \mathcal{J}^- & 0\\ 0 & 0 & 0\end{pmatrix}, \quad (2.48)$$

where $\mathcal{J}^\pm \equiv \cos^2(\varphi)(J_0 \pm J_2) + \sin^2(\varphi)(J_0 \mp J_2)$ and $J_m \equiv J_m(k_\parallel R)$ is the Bessel function of the first kind, and, for p-polarization,

$$\left\langle \hat{\varepsilon}^{(\mathrm{p})}(\hat{\mathbf{k}}_m^{(\sigma_2)})\hat{\varepsilon}^{(\mathrm{p})}(\hat{\mathbf{k}}_l^{(\sigma_1)})\right\rangle = \frac{1}{2k_m k_l} \times \begin{pmatrix} \sigma_1\sigma_2 k_{zm}k_{zl}\mathcal{J}^- & -\sigma_1\sigma_2 k_{zm}k_{zl}J_2\sin(2\varphi) & -\sigma_1 2\mathrm{i}k_{zm}k_\parallel J_1\cos(\varphi)\\ -\sigma_1\sigma_2 k_{zm}k_{zl}J_2\sin(2\varphi) & \sigma_1\sigma_2 k_{zm}k_{zl}\mathcal{J}^+ & -\sigma_1 2\mathrm{i}k_{zm}k_\parallel J_1\sin(\varphi)\\ -\sigma_2 2\mathrm{i}k_{zl}k_\parallel J_1\cos(\varphi) & -\sigma_2 2\mathrm{i}k_{zl}k_\parallel J_1\sin(\varphi) & 2k_\parallel^2 J_0\end{pmatrix}, \quad (2.49)$$

where $k_i = \sqrt{k_\parallel^2 + k_{zi}} = \omega/c_i'$.

$P(\mathbf{k}_\parallel)$	$\int \mathrm{d}\varphi_{\mathbf{k}_\parallel} P(\mathbf{k}_\parallel)\exp(\mathrm{i}\mathbf{k}_\parallel\cdot\mathbf{R})$
1	$2\pi J_0$
k_x	$2\mathrm{i}\pi k_\parallel\cos(\varphi)J_1$
k_y	$2\mathrm{i}\pi k_\parallel\sin(\varphi)J_1$
k_x^2	$\pi k_\parallel^2[\cos^2(\varphi)(J_0-J_2)+\sin^2(\varphi)(J_0+J_2)]$
k_xk_y	$-\pi k_\parallel^2\sin(2\pi)J_2$
k_y^2	$\pi k_\parallel^2[\cos^2(\varphi)(J_0+J_2)+\sin^2(\varphi)(J_0-J_2)]$

Table 2.2: Angular wavevector integrals and their corresponding anti-derivatives, used to evaluate Eq. (2.42). We use the coordinates $\mathbf{k}_\parallel = (k_\parallel, \varphi_{\mathbf{k}_\parallel})$ and $\mathbf{R} = (R,\varphi)$, and the shorthand $J_m \equiv J_m(k_\parallel R)$. Adopted from Ref. 27.

2.4.2 The Field of a Point Dipole

Point dipoles are, as previously mentioned, a common way to excite SPPs, since they in the near field produce evanescent waves with large momentum. To incorporate a dipole into our Green's function formalism, we simply need to know its current density. For a point dipole located at $\mathbf{r}_0$ in frequency domain with a dipole moment of $\mathbf{p}$, the current density at $\mathbf{r}$ is simply

$$\mathbf{j} = -\mathrm{i}\omega\mathbf{p}\delta(\mathbf{r}-\mathbf{r}_0), \quad (2.50)$$

having used that $\mathbf{j} = \partial_t \mathbf{P}$ and that the polarization density of a point dipole is $\mathbf{P} = \mathbf{p}\delta(\mathbf{r} - \mathbf{r}_0)$. We can then insert this into Eq. (2.38) to acquire the well known result [9]

$$\mathbf{E}_\omega(\mathbf{r}) = \frac{\mu_r}{\varepsilon_0} k_0^2 \mathbf{G}(\mathbf{r}, \mathbf{r}_0) \cdot \mathbf{p}, \tag{2.51}$$

where $k_0 = \omega/c$. The above expression, in combination with Eq. (2.47), allows us to calculate the total electric field produced by a dipole near an arbitrary stratified structure. As an example, we can calculate the enhanced decay rate of a dipole, which is given by [9]

$$\Gamma/\Gamma_0 = 1 + \frac{6\pi\varepsilon_0}{k_0^3 |\mathbf{p}|^2} \mathrm{Im}\{\mathbf{p}^* \cdot \mathbf{E}_\omega\}, \tag{2.52}$$

where $*$ is the complex conjugate and we have normalized with respect to the free space decay rate $\Gamma_0 = \mu_r \omega k_0^3 |\mathbf{p}|^2 / 12\pi\varepsilon_0$. By inserting Eq. (2.51), this reduces to

$$\Gamma/\Gamma_0 = 1 + \frac{6\pi\mu_r}{k_0} \mathrm{Im}\{\hat{\mathbf{p}}^* \cdot \mathbf{G}(\mathbf{r}, \mathbf{r}_0) \cdot \hat{\mathbf{p}}\}. \tag{2.53}$$

The enhanced decay rate, or Purcell factor, is a measure for how much more power is dissipated when the dipole is placed near a photonic environment. The above expression is the total dissipated power, meaning it does not discriminate how much power is radiated away, absorbed by the material or converted to plasmons. In Fig. 2.12(a), we calculate the Purcell factor for a dipole placed 10 nm above a graphene sheet and in Fig. 2.12(b) a dipole in between two sheets. It is clear that the dipole couples strongly with the graphene sheet, the emission rate being enhanced between 1−5 orders of magnitude. The addition of a second sheet increases this slightly more and narrows the peak. Furthermore, we notice the onset of interband damping at higher frequencies

Importantly, besides enhancing its own decay rate, the interaction with the nearby structure provokes a self-illumination of the dipole by its own radiated field. To model the innate polarizability of the dipole α we use [10]

$$\alpha = 4\pi\varepsilon_2 r_\alpha^3 \frac{\varepsilon_1 - \varepsilon_2}{\varepsilon_1 + 2\varepsilon_2}, \tag{2.54}$$

where ε_2 is the permittivity of the material of the dipole, ε_2 is the permittivity of the environment and r_α is an effective radius. For the rest of this work, we use Eq. (2.30) to model the permittivity of the dipole, using the same parameters as in Fig. 2.5 and assume an effective radius of $r_\alpha = 15$ nm, unless specified otherwise. Assuming we illuminate the dipole with some external field $\mathbf{E}_{\text{ext}}$, the dipole moment is then given by

$$\mathbf{p} = \alpha\left(\mathbf{E}_{\text{ext}} + \frac{\mu_r}{\varepsilon_0} k_0^2 \mathbf{G}(\mathbf{r}_0, \mathbf{r}_0) \cdot \mathbf{p}\right), \tag{2.55}$$

where we have included the contribution from the dipole acting back on itself. Isolating $\mathbf{p}$ gives us

$$\mathbf{p} = \alpha\left[\mathbb{I} - \frac{\mu_r}{\varepsilon_0} \alpha k_0^2 \mathbf{G}(\mathbf{r}_0, \mathbf{r}_0)\right]^{-1} \cdot \mathbf{E}_{\text{ext}} = \alpha_{\text{eff}} \cdot \mathbf{E}_{\text{ext}}, \tag{2.56}$$

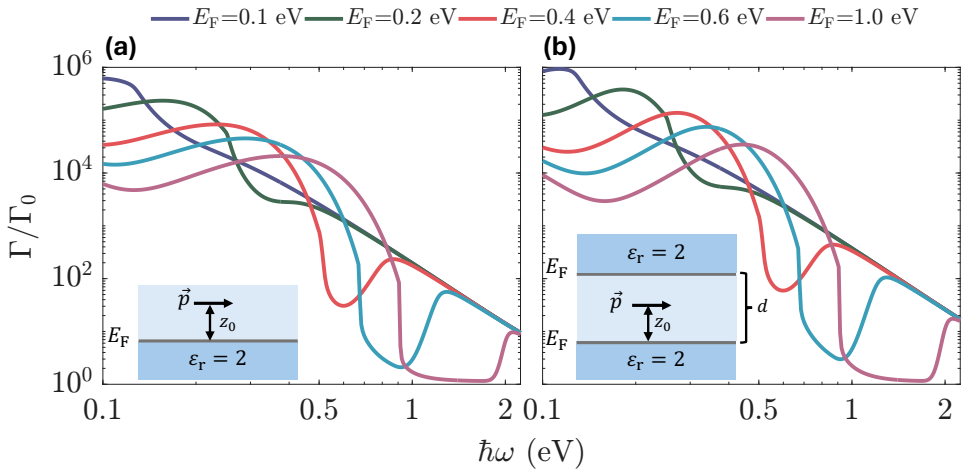

Figure 2.12: Purcell enhancement of a point dipole when placed near a graphene sheet, normalized to free space, as a function of frequency. **(a)** A single graphene sheet is placed below a dipole, reproducing the results of Ref. 16. **(b)** A second graphene sheet is added above the dipole, giving the medium of the dipole a thickness of $d = 20$ nm. In both systems, the dipole is in vacuum and the second material is modeled with $\varepsilon_r = 2$. The dipole is placed $z_0 = 10$ nm above the first sheet and is polarized in parallel with the interface. We used a carrier mobility of $\mu_M = 10^4$ cm^2/Vs and the non-local RPA conductivity model to describe the graphene, along with the Fermi level values indicated in the legend.

where $\mathbb{I}$ is the identity matrix and the negative power of the parentheses should be understood as the inverse matrix. We observe that the optical response of the dipole to the external field is well captured by an effective polarizability defined as

$$\alpha_{\text{eff}} \equiv \alpha\left[\mathbb{I} - \frac{\mu_r}{\varepsilon_0}\alpha k_0^2 \mathbf{G}(\mathbf{r}_0, \mathbf{r}_0)\right]^{-1}, \tag{2.57}$$

which captures the interaction between the dipole and the structure through $\mathbf{G}(\mathbf{r}_0, \mathbf{r}_0)$.

Far Field of Dipole and Photon Count

In practice, when measuring the field of e.g. a dipole, the detector is often placed far away from the source, and is therefore only sensitive to the emitted far field, which behaves as a spherical wave. In this case, the far-field at $\mathbf{r}$ of a dipole at $\mathbf{r}_0$ can be written as

$$\mathbf{E}(\mathbf{r}) = \mathbf{f}\frac{e^{ik|\mathbf{r}-\mathbf{r}_0|}}{|\mathbf{r}-\mathbf{r}_0|}, \tag{2.58}$$

where we have assumed the dipole and detector are in the same medium and we introduce the far-field amplitude

$$\mathbf{f} = \frac{k^2}{4\pi\varepsilon_0}[\mathbf{p} - \hat{\mathbf{r}}(\mathbf{p}\cdot\hat{\mathbf{r}})]. \tag{2.59}$$

Next, we split the field into s- and p-polarized components

$$\mathbf{f} = f_s\hat{\varepsilon}^{(s)} + f_p\hat{\varepsilon}^{(p)} \tag{2.60}$$

where

$$f_{\mathrm{s}} = \frac{k^2}{4\pi\varepsilon_0}\hat{\varepsilon}^{(\mathrm{s})}\left[1 + r^{(\mathrm{s})}(\theta,\omega)\mathrm{e}^{-2\mathrm{i}k_z z_0}\right]\cdot\mathbf{p}, \tag{2.61a}$$

$$f_{\mathrm{p}} = \frac{k^2}{4\pi\varepsilon_0}\left[\hat{\varepsilon}^{(\mathrm{p},+)} + \hat{\varepsilon}^{(\mathrm{p},-)}r^{(\mathrm{p})}(\theta,\omega)\mathrm{e}^{-2\mathrm{i}k_z z_0}\right]\cdot\mathbf{p}, \tag{2.61b}$$

and we assume the dipole is located in vacuum and that $z_0 < 0$. The polarization vectors are given by Eq. (2.41), and it is useful to express them in spherical coordinates

$$\begin{aligned} k_x &= k\sin\theta\cos\varphi, \\ k_y &= k\sin\theta\sin\varphi, \\ k_z &= k\cos\theta, \\ k_\parallel &= \sqrt{k_x^2 + k_y^2} = k\sin\theta, \end{aligned}$$

so we can write their tensor products as

$$\hat{\varepsilon}^{(\mathrm{s})}\otimes\hat{\varepsilon}^{(\mathrm{s})} = \begin{pmatrix} \sin^2\varphi & -\sin\varphi\cos\varphi & 0 \\ -\sin\varphi\cos\varphi & \cos^2\varphi & 0 \\ 0 & 0 & 0 \end{pmatrix}, \tag{2.62a}$$

$$\hat{\varepsilon}^{(p,+)}\otimes\hat{\varepsilon}^{(p,\pm)} = \begin{pmatrix} \pm\cos^2\theta\cos^2\varphi & \pm\cos^2\theta\cos\varphi\sin\varphi & -\cos\theta\cos\varphi\sin\theta \\ \pm\cos^2\theta\cos\varphi\sin\varphi & \pm\cos^2\theta\sin^2\varphi & -\cos\theta\sin\varphi\sin\theta \\ \mp\cos\theta\cos\varphi\sin\theta & \mp\cos\theta\sin\varphi\sin\theta & \sin^2\theta \end{pmatrix}. \tag{2.62b}$$

Using these tensors, we write the far field as

$$\mathbf{f}(\theta,\varphi,\omega) = (\mathbf{f}_{\mathrm{s}} + \mathbf{f}_{\mathrm{p}})\cdot\mathbf{p}, \tag{2.63}$$

where

$$\mathbf{f}_{\mathrm{s}} = \frac{k^2}{4\pi\varepsilon_0}\left[1 + r^{(\mathrm{s})}(\theta,\omega)\mathrm{e}^{-2\mathrm{i}k_z z_0}\right]\hat{\varepsilon}^{(\mathrm{s})}\otimes\hat{\varepsilon}^{(\mathrm{s})}, \tag{2.64a}$$

$$\mathbf{f}_{\mathrm{p}} = \frac{k^2}{4\pi\varepsilon_0}\left[\hat{\varepsilon}^{(\mathrm{p},+)}\otimes\hat{\varepsilon}^{(\mathrm{p},+)} + r^{(\mathrm{p})}(\theta,\omega)\mathrm{e}^{-2\mathrm{i}k_z z_0}\hat{\varepsilon}^{(\mathrm{p},+)}\otimes\hat{\varepsilon}^{(\mathrm{p},-)}\right], \tag{2.64b}$$

where it should be understood that $\mathbf{f}_{\mathrm{s}}$ and $\mathbf{f}_{\mathrm{p}}$ are 3×3 matrices. The reflection coefficients used are obtained either from Eqs (2.14) and (2.16) or by use of the transfer matrix method presented in Appendix A.

Finally, the total power radiated by the dipole per unit of solid angle, in terms of the far field, is given by [27]

$$\frac{\mathrm{d}P}{\mathrm{d}\Omega} = \frac{1}{2}\sqrt{\varepsilon_{\mathrm{r}}}c|\mathbf{f}(\theta,\varphi,\omega)|^2, \tag{2.65}$$

and the emission rate is then

$$\Gamma_{\mathrm{count}} = \frac{1}{2}\frac{\sqrt{\varepsilon_{\mathrm{r}}}c}{\hbar\omega}\int_0^{2\pi}\mathrm{d}\varphi\int_0^{\pi/2}\mathrm{d}\theta|\mathbf{f}(\theta,\varphi,\omega)|^2\sin\theta. \tag{2.66}$$

It should be noted, that in practice, a detector would not cover the whole space above the emitter, and so we should not integrate over all θ angles. However, for simplicity we will stick with these bounds.

2.4.3 Green's Function for Spatially Uniform Source

Finally, we want to determine the electric field of a spatially uniform source. We recall that the electric field and the Green's function were related by a spatial integral in Eq. (2.38) and that the general Green's function for a stratified structure was given by Eq. (2.42). If the current density is spatially uniform, and therefore independent of $\mathbf{r}'$, we can immediately perform the integral in Eq. (2.38), using that

$$2\pi\delta(k_x) = \int_{-\infty}^{\infty} \mathrm{d}x' \mathrm{e}^{-\mathrm{i}k_x x'}, \tag{2.67}$$

and likewise for y'. These Dirac-delta functions then trivialize the two wavevector integrals to yield

$$\begin{aligned}\int \mathrm{d}^3\mathbf{r}' G_{ij}(z,\mathbf{r}') = &-\frac{\hat{z}_i\hat{z}_j}{k_m^2} \\ &+ \frac{\mathrm{i}}{2}\sum_{\nu=\mathrm{s,p}}\sum_{\substack{\sigma_1=\pm\\ \sigma_2=\pm}}\int_{-\infty}^{\infty}\mathrm{d}z'\frac{1}{k_l}A_{lm}^{(\sigma_1,\sigma_2,\nu)}(k_\parallel=0,z,z')\lim_{k_\parallel\to 0}\hat{\varepsilon}_i^{(\nu)}(\hat{\mathbf{k}}_m^{(\sigma_2)})\hat{\varepsilon}_j^{(\nu)}(\hat{\mathbf{k}}_l^{(\sigma_1)}),\end{aligned} \tag{2.68}$$

where, for each z and z' we must choose the layers l and m accordingly. From the Dirac delta above, we further obtain that $k_{lz} = k_l$ for $k_\parallel = 0$.

To reduce the second term in Eq. (2.68), we first note it can be shown that, for $k_\parallel = 0$, the s- and p-polarized Fresnel coefficients are related by

$$r^{(\mathrm{s})} = -r^{(\mathrm{p})}, \tag{2.69a}$$
$$t^{(\mathrm{s})} = t^{(\mathrm{p})}. \tag{2.69b}$$

Using this and inspecting Table 2.1, we can determine the relation between the s- and p-polarized amplitude coefficients, in the $k_\parallel = 0$ limit, as

$$A_{lm}^{(+,-,\mathrm{s})} = -A_{lm}^{(+,-,\mathrm{p})}, \tag{2.70a}$$
$$A_{lm}^{(+,+,\mathrm{s})} = A_{lm}^{(+,+,\mathrm{p})}, \tag{2.70b}$$
$$A_{lm}^{(-,+,\mathrm{s})} = -A_{lm}^{(-,+,\mathrm{p})}, \tag{2.70c}$$
$$A_{lm}^{(-,-,\mathrm{s})} = A_{lm}^{(-,-,\mathrm{p})}. \tag{2.70d}$$

Finally, for the polarizability vectors, it can be shown that

$$\lim_{k_\parallel\to 0}\left[\hat{\varepsilon}^{(\mathrm{s})}(\hat{\mathbf{k}}^{(\pm)})\hat{\varepsilon}^{(\mathrm{s})}(\hat{\mathbf{k}}_l^{(\pm)}) + \hat{\varepsilon}^{(\mathrm{p})}(\hat{\mathbf{k}}^{(\pm)})\hat{\varepsilon}^{(\mathrm{p})}(\hat{\mathbf{k}}_l^{(\pm)})\right] = \begin{pmatrix}1&0&0\\0&1&0\\0&0&0\end{pmatrix}, \tag{2.71}$$

for the $(+,+)$ and $(-,-)$ case. When the signs mix we instead have

$$\lim_{k_\parallel\to 0}\left[\hat{\varepsilon}^{(\mathrm{s})}(\hat{\mathbf{k}}^{(\pm)})\hat{\varepsilon}^{(\mathrm{s})}(\hat{\mathbf{k}}_l^{(\mp)}) - \hat{\varepsilon}^{(\mathrm{p})}(\hat{\mathbf{k}}^{(\pm)})\hat{\varepsilon}^{(\mathrm{p})}(\hat{\mathbf{k}}_l^{(\mp)})\right] = \begin{pmatrix}1&0&0\\0&1&0\\0&0&0\end{pmatrix}, \tag{2.72}$$

i.e. the p-polarized tensor need to flip sign to be able to add to "unity" with the s-polarized tensor, like the same sign case. Luckily, this is fixed exactly by Eq. (2.70a) and (2.70c), while Eq. (2.70b) and (2.70d) allows us to add the same sign tensors with no issue. Equation (2.68) now reduces to

$$\int \mathrm{d}^3\mathbf{r}' G_{ij}(z,\mathbf{r}') = -\frac{\hat{z}_i\hat{z}_j}{k_m^2} + \frac{\mathrm{i}}{2}\sum_{\substack{\sigma_1=\pm\\ \sigma_2=\pm}}\int_{-\infty}^{\infty}\mathrm{d}z'\frac{1}{k_l}A_{lm}^{(\sigma_1,\sigma_2,\mathrm{s})}(k_\parallel=0,z,z')(\hat{x}_i\hat{x}_j+\hat{y}_i\hat{y}_j). \quad (2.73)$$

The remaining z' integral is in practice a sum of integrals, each with their own set of bounds, to account for varying thickness of the layers

$$\int_{-\infty}^{\infty}\mathrm{d}z' \to \sum_{l=1}^{N}\int_{z_l}^{z_{l+1}}\mathrm{d}z'. \quad (2.74)$$

From inspecting Table 2.1, we can identify four different types of integrals, the first two being

$$\int_{z_l}^{z_{l+1}}\mathrm{d}z'\Delta_l^{\pm} = \frac{\mathrm{i}}{k_l}(1-\Delta_l). \quad (2.75)$$

The last two types are from the direct field, involving the Heaviside function. For the $(+,+)$ case the integral becomes

$$\int_{z_l}^{z_{l+1}}\mathrm{e}^{\mathrm{i}k_l(z-z')}\Theta(z-z') = \frac{\mathrm{i}}{k_l}\Big(1-\mathrm{e}^{\mathrm{i}k_l(z-z_l)}\Big), \quad (2.76)$$

and for the $(-,-)$ we get

$$\int_{z_l}^{z_{l+1}}\mathrm{e}^{-\mathrm{i}k_l(z-z')}\Theta(z'-z) = \frac{\mathrm{i}}{k_l}\Big(1-\mathrm{e}^{\mathrm{i}k_l(z_{l+1}-z)}\Big). \quad (2.77)$$

The Green's function for a spatially uniform source, near a N-layered structure, can finally be written as

$$\int \mathrm{d}^3\mathbf{r}' G_{ij}(z,\mathbf{r}') = -\frac{\hat{z}_i\hat{z}_j}{k_m^2} + \frac{\mathrm{i}}{2}\sum_{\substack{\sigma_1=\pm\\ \sigma_2=\pm}}\sum_{l}^{N}\frac{1}{k_l}\tilde{A}_{lm}^{(\sigma_1,\sigma_2,\mathrm{s})}(z)(\hat{x}_i\hat{x}_j+\hat{y}_i\hat{y}_j), \quad (2.78)$$

where the integrated amplitude coefficients are given in Table 2.3.

	$l>m$	$l<m$	$l=m$
$\tilde{A}_{lm}^{(+,-,\mathrm{s})}$	$\Lambda^{(\mathrm{s})}\delta_l\tilde{r}_{lN}^{(\mathrm{s})}\Delta_l\Delta_m^{+}$	$\Lambda^{(\mathrm{s})}\delta_l\Delta_m\tilde{r}_{mN}^{(\mathrm{s})}\Delta_m^{+}$	$\frac{\delta_l\tilde{r}_{mN}^{(\mathrm{s})}\Delta_m^{+}}{1-\tilde{r}_{mN}^{(\mathrm{s})}\tilde{r}_{mN}^{(\mathrm{s})}\Delta_m^2}$
$\tilde{A}_{lm}^{(+,+,\mathrm{s})}$	$\Lambda^{(\mathrm{s})}\delta_l\tilde{r}_{lN}^{(\mathrm{s})}\Delta_l\Delta_m\tilde{r}_{m1}\Delta_m^{-}$	$\Lambda^{(\mathrm{s})}\delta_l\Delta_m^{-}$	$\frac{\mathrm{i}}{k_l}\Big(1-\Delta_l^{-}\Big)+\frac{\delta_l\tilde{r}_{mN}^{(\mathrm{s})}\Delta_m\tilde{r}_{m1}^{(\mathrm{s})}\Delta_m^{-}}{1-\tilde{r}_{mN}^{(\mathrm{s})}\tilde{r}_{mN}^{(\mathrm{s})}\Delta_m^2}$
$\tilde{A}_{lm}^{(-,+,\mathrm{s})}$	$\Lambda^{(\mathrm{s})}\delta_l\Delta_m\tilde{r}_{m1}^{(\mathrm{s})}\Delta_m^{-}$	$\Lambda^{(\mathrm{s})}\delta_l\tilde{r}_{l1}^{(\mathrm{s})}\Delta_l\Delta_m^{-}$	$\frac{\delta_l\tilde{r}_{m1}^{(\mathrm{s})}\Delta_m^{-}}{1-\tilde{r}_{mN}^{(\mathrm{s})}\tilde{r}_{mN}^{(\mathrm{s})}\Delta_m^2}$
$\tilde{A}_{lm}^{(-,-,\mathrm{s})}$	$\Lambda^{(\mathrm{s})}\delta_l\Delta_m^{+}$	$\Lambda^{(\mathrm{s})}\delta_l\tilde{r}_{l1}^{(\mathrm{s})}\Delta_l\Delta_m\tilde{r}_{mN}^{(\mathrm{s})}\Delta_m^{+}$	$\frac{\mathrm{i}}{k_l}\Big(1-\Delta_l^{+}\Big)+\frac{\delta_l\tilde{r}_{m1}^{(\mathrm{s})}\Delta_m\tilde{r}_{mN}^{(\mathrm{s})}\Delta_m^{+}}{1-\tilde{r}_{mN}^{(\mathrm{s})}\tilde{r}_{mN}^{(\mathrm{s})}\Delta_m^2}$

Table 2.3: Amplitude coefficients integrated over z', where we have defined $\delta_l \equiv \frac{\mathrm{i}}{k_l}(1-\Delta_l)$.

Finally, it should be noted that the field resulting from a spatially uniform source, which later will be the axion field, cannot directly excite plasmons in an extended system. This is due to the Dirac-delta function forcing the in-plane momentum to zero. In contrast to a point dipole source, a uniform field is completely delocalized, meaning its momentum is strictly within the light cone. However, as we have seen from Eq. (2.56), such a field can still excite a dipole, which in turn may couple with the GSPPs. The exact system will discussed more in depth in the following chapter.

Chapter 3

Axion Electrodynamics

Having established the necessary theory of classical electrodynamics, we now want to incorporate the interactions with *axions*. These are theoretical elementary particles, with an unknown coupling to light and mass, that may be a component of cold dark matter and solve the strong CP problem. Being a light boson, we can describe the axion as a classical field, similar to light, with a wavelength often exceeding the "lab frame" [6]. Fig. 3.1 shows a map over possible coupling constants and masses for the axion and combinations that has already been ruled out by experiments or astrophysical observations. The yellow, linear,"belt" represents possible combinations of coupling and mass for the axion which would solve the strong CP problem, called QCD axions, and are therefore of special interest. The rest of the space represent axion-like particles (ALPs), that would still be viable dark matter candidates. In this work we will focus on masses of $m_{\mathrm{a}}c^2 \sim 10^{-2} - 10^{0}$ eV and couplings of $g_{\mathrm{a}}/\hbar \sim 10^{-10}$ GeV^{-1}.

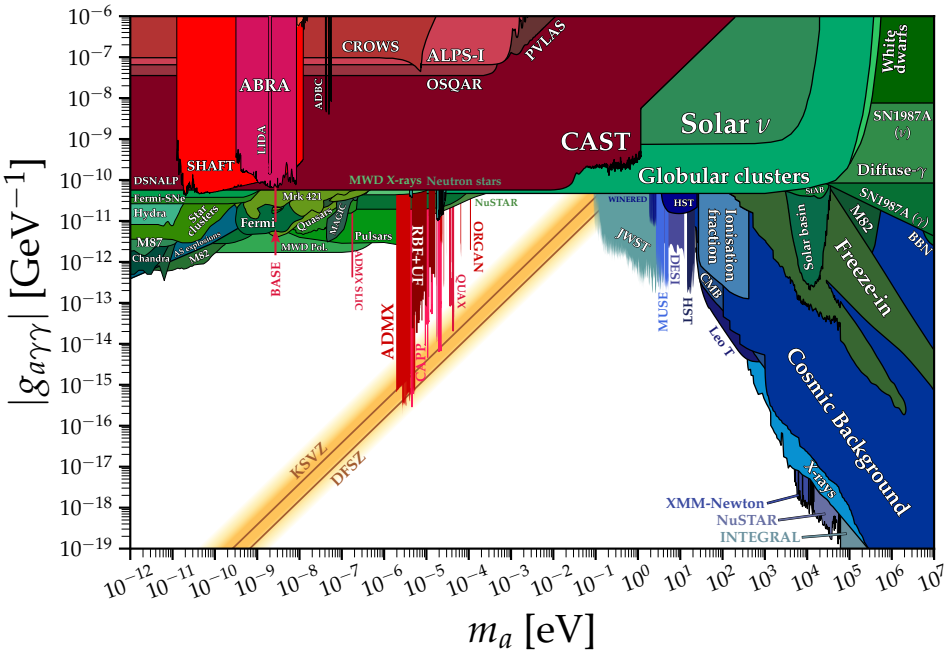

Figure 3.1: Limits of the axion-photon coupling and axion mass [28].

3.1 Modified Maxwell Equations

It was shown in 1983 by P. Sikivie [29] that the existence of axions would modify the traditional Maxwell equations, enabling the development of optics-based detection methods. Specifically, in the presence of a strong magnetic field, axions can convert into photons which then can be detected. Within this description, axions are regarded as a field $a(\mathbf{r}, t)$ that can be incorporated into traditional electrodynamics by writing the combined action of classical electromagnetism and an interacting scalar field [30]

$$S[A, a] = \int \mathrm{d}^4x \left(-\frac{1}{4\mu_0} F_{\mu\nu}F^{\mu\nu} - A_\mu j^\mu - \frac{g_\mathrm{a}}{4\mu_0} a F_{\mu\nu}\tilde{F}^{\mu\nu} + \frac{\hbar}{2c}\partial_\mu a^* \partial^\mu a - \frac{c}{2\hbar} m_\mathrm{a}^2 |a|^2 \right), \tag{3.1}$$

where the first two terms constitute the classical Maxwell Lagrangian density, the last two are the kinetic and potential axion terms, respectively, and the third term describes the interaction between the photon and axion. The field strength tensor follows as $F_{\mu\nu} = \partial_\mu A_\nu - \partial_\nu A_\mu$, where $A^\mu = (\phi/c, \mathbf{A})$ is the four-vector potential with ϕ being the electric scalar potential and $\mathbf{A}$ the magnetic vector potential, while $j^\mu = (c\rho_\mathrm{tot}, \mathbf{j}_\mathrm{tot})$ is the four-current. The interaction term includes both the axion-photon coupling, g_a, the axion field a and the dual tensor $\tilde{F}^{\mu\nu}$, while the the kinetic and potential, naturally, include the four-derivative, $\partial_\mu = (\partial_t/c, \nabla)$, and the axion mass, m_a, respectively. Finally, the axion field is complex with dimensions of inverse time, while the coupling has units of time, such that $g_\mathrm{a} a$ is dimensionless.

The equations of motion are obtained by minimizing the action, i.e. using the Euler-Lagrange equation

$$\partial_\mu \left(\frac{\partial \mathcal{L}}{\partial(\partial_\mu A_\nu)} \right) - \frac{\partial \mathcal{L}}{\partial A_\nu} = 0, \tag{3.2}$$

and similarly for a and a^*. The resulting five equations are

$$\nabla \cdot \mathbf{D} = \rho - \frac{g_\mathrm{a}}{Z_0} \mathbf{B} \cdot \nabla a, \tag{3.3a}$$

$$\nabla \cdot \mathbf{B} = 0, \tag{3.3b}$$

$$\nabla \times \mathbf{E} = -\partial_t \mathbf{B}, \tag{3.3c}$$

$$\nabla \times \mathbf{H} = \mathbf{j} + \partial_t \mathbf{D} + \frac{g_\mathrm{a}}{Z_0} (\mathbf{B}\partial_t a - \mathbf{E} \times \nabla a), \tag{3.3d}$$

$$\Box a + \frac{c^2 m_\mathrm{a}^2}{\hbar^2} a = \frac{2 g_\mathrm{a}}{\hbar \mu_0} \mathbf{E} \cdot \mathbf{B}, \tag{3.3e}$$

where $Z_0 = \sqrt{\mu_0/\varepsilon_0}$ is the vacuum wave impedance and Eq. (3.3e) is the axion field equation of motion with $\Box = \partial_t^2/c^2 - \nabla^2$ being the d'Alembert operator. As with the traditional Maxwell equations, we can likewise for the modified ones derive the corresponding wave equations. Taking the curl on both sides of Eq. (3.3c) and substituting in Eq. (3.3d) gives us the wave equation for the electric field

$$\nabla^2 \mathbf{E} - \varepsilon\mu\partial_t^2 \mathbf{E} = \nabla(\nabla \cdot \mathbf{E}) + \mu\partial_t \mathbf{j} + \frac{g_\mathrm{a}}{Z_0} \mu \partial_t (\mathbf{B}\partial_t a + \nabla a \times \mathbf{E}), \tag{3.4}$$

and simply taking the curl of Eq. (3.3d) gives us the wave equation of $\mathbf{H}$

$$\nabla^2\mathbf{H} - \varepsilon\mu\partial_t^2\mathbf{H} = -\nabla\times\mathbf{j} - \frac{g_\mathrm{a}}{Z_0}\nabla\times(\mathbf{B}\partial_t a + \nabla a\times\mathbf{E}). \tag{3.5}$$

From above equations it becomes clear that, under the right circumstances, the axion field can act as a source for $\mathbf{E}$- and $\mathbf{H}$-fields.

3.1.1 Axions as Photon Sources

As is common practice, we will consider cold dark matter axions, meaning that their velocity is around $v_\mathrm{a} = 10^{-3}c$ and their de Broglie wavelength,

$$\lambda_\mathrm{a} = \frac{2\pi\hbar}{m_\mathrm{a}v_\mathrm{a}}, \tag{3.6}$$

is large enough ($\lambda_\mathrm{a} \sim 1-100$ mm for $m_\mathrm{a}c^2 \sim 0.01-1$ eV), compared with the laboratory framework, such that we can take $\nabla a \approx 0$ [31]. The large wavelength of axions, and the fact that they are bosons, is also the reason why we treat them as a classical wave, rather than a particle like electrons.

Our system will be illuminated by a strong, static and spatially uniform magnetic field $\mathbf{B}_0$, such that the modified wave equations can be written as

$$\nabla^2\mathbf{E} - \varepsilon\mu\partial_t^2\mathbf{E} = \nabla(\nabla\cdot\mathbf{E}) + \mu\partial_t\mathbf{j} + \mu\partial_t\mathbf{j}_\mathrm{a}, \tag{3.7a}$$

$$\nabla^2\mathbf{H} - \varepsilon\mu\partial_t^2\mathbf{H} = -\nabla\times\mathbf{j}, \tag{3.7b}$$

where the axion current is defined as

$$\mathbf{j}_\mathrm{a} = \frac{g_\mathrm{a}}{Z_0}\mathbf{B}_0\partial_t a. \tag{3.8}$$

Since both $\mathbf{B}_0$ and $a(t)$ are spatially uniform, and the spatially varying induced fields are insignificant compared to $\mathbf{B}_0$, we can use the formulation presented in Sec. 2.4.3 to calculate the related electric field.

We will assume that the axion field is described by an amplitude a_0 and frequency ω in the form [32]

$$a(t) = a_0\mathrm{e}^{-\mathrm{i}\omega t}, \tag{3.9}$$

and working with time-harmonic fields, all fields oscillate with this frequency. The mass of the axion can be related to its frequency through the Compton relation

$$\omega = \frac{m_\mathrm{a}c^2}{\hbar}, \tag{3.10}$$

such that, to determine the magnitude of the axion current for a given B-field and axion mass, we only need the axion field's amplitude a_0. An expression for this can be obtained through the stress-energy (SE) tensor which, for a complex scalar field, is defined as [33]

$$T^\mu_\nu = \frac{\partial\mathcal{L}_\mathrm{a}}{\partial(\partial_\mu a)}\partial_\nu a + \frac{\partial\mathcal{L}_\mathrm{a}}{\partial(\partial_\mu a^*)}\partial_\nu a^* - \delta^\mu_\nu\mathcal{L}_\mathrm{a}, \tag{3.11}$$

where, since we want the energy density for the axion field, we have only included the axion term of the Lagrangian

$$\mathcal{L}_{\mathrm{a}} = \frac{\hbar}{2c}\partial_\mu a^* \partial^\mu a - \frac{c}{2\hbar} m_{\mathrm{a}}^2 |a|^2. \tag{3.12}$$

The $\mu = 0,\ \nu = 0$ component of the SE tensor is the energy density of the field, and, reducing Eq. (3.11), we get

$$T^{00} \equiv \rho_{\mathrm{a}} = \frac{c}{\hbar} m_{\mathrm{a}}^2 |a_0|^2, \tag{3.13}$$

where we have used Eq. (3.10) to relate the mass and frequency. Finally, the axion amplitude is given by

$$|a_0| = \sqrt{\frac{\hbar \rho_{\mathrm{a}}}{m_{\mathrm{a}}^2 c}}, \tag{3.14}$$

where the energy density for local cold dark matter is estimated to be [34]

$$\rho_{\mathrm{a}} = 0.3\ \frac{\mathrm{GeV}}{\mathrm{cm}^3}. \tag{3.15}$$

To summarize, for some photonic environment, the electric field produced by the axion field is given by Eqs. (2.38),

$$E_{\omega,i}(z) = \mathrm{i}\omega j_{\mathrm{a},j} \int \mathrm{d}^3\mathbf{r}' G_{ij}(z, \mathbf{r}'), \tag{3.16}$$

where the Green's function is given by Eq. (2.78) and the source is

$$j_{\mathrm{a},i} = \frac{g_{\mathrm{a}}}{Z_0} \omega a_0 B_{0,i}. \tag{3.17}$$

3.2 Axions in Nanophotonics

In this section we will examine whether nanostructures can work as optical platforms for axion detection, using the framework developed in the previous sections. Throughout this section, we will be using a axion-photon coupling of $g_{\mathrm{a}}/\hbar = 10\ \mathrm{GeV}^{-1}$, the axion density given by Eq. (3.15) and a magnetic field given by $\mathbf{B}_0 = B_0\hat{\mathbf{x}}$ with $B_0 = 10$ T, following commonly reported values from the literature [35, 36]. Finally, we note that we assume throughout the upcoming results that the optical resonances we target are always resonant with the axion field. This means that, when we present some plot as a function of frequency, we are implicitly sweeping over axion masses, m_{a}, since through Eq. (3.10) we can treat mass and frequency as the same quantity. In practice, we expect that axions of a given mass will resonate with our structure only at that specific frequency and not the rest of the spectrum.

3.2.1 Axion Detection in Extended Systems

In this section, we consider some planar optical structures capable of supporting low-frequency resonances of the order $\sim 0.1-1$ eV. Specifically, we consider stacks of graphene sheets over which we place a point dipole. The purpose of the latter (which in practice represents a nanoparticle or a tip) is to interact with the background axion current –which we take to be uniform under a static magnetic field– and excite the plasmon modes of the nearby structure. The generated strong plasmonic near fields then act back on the dipole, which can radiate photons into the far field. This radiation has two components: direct dipole emission and the feedback through the photonic system. Ideally, the strong plasmonic fields can amplify the latter contribution into photon counts large enough to be detected in the far field.

We start by considering the case of a dipole placed above a stack of $N_{\rm GS} = 1-3$ graphene sheets separated by a uniform distance, as shown in the inset of Fig. 3.2(b). We describe this system using the formalism presented in Chapter 2: we use the transfer matrix formalism to describe the optical response of the stack, then we use the Green's function formalism to compute the axion current in such system, and finally we use the dipole theory to estimate the subsequent emission photon counts.

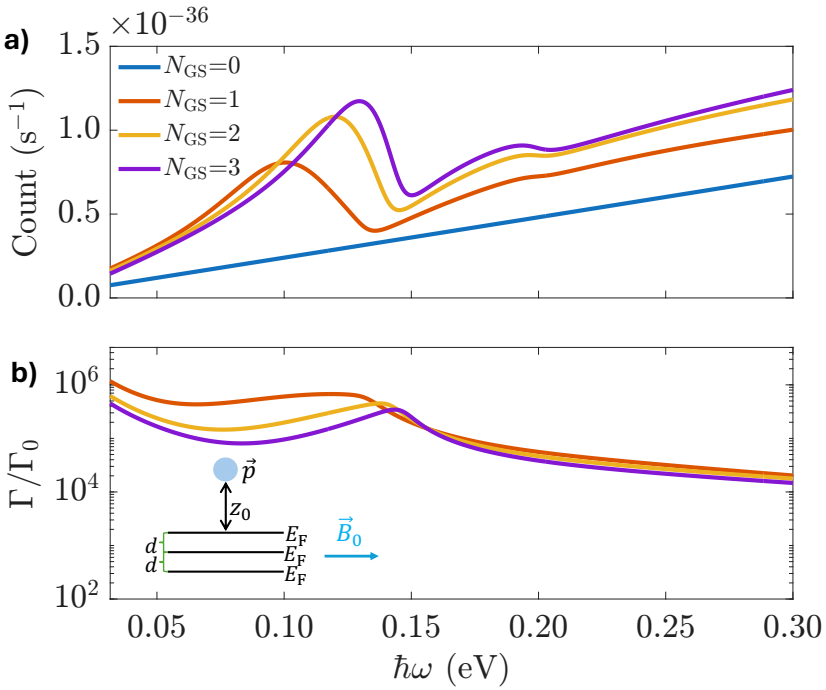

Figure 3.2: **(a)** The photon count, Eq. (2.66), for different number of graphene sheets, $N_{\rm GS}$, when a dipole described by Eq. (2.57) , with an effective radius of $r_\alpha = 15$ nm, is placed $z_0 = 10$ nm above the first interface and is driven by the axion current Eq. (3.17). **(b)** The corresponding Purcell enhancement given by Eq. (2.53). The graphene sheets all have a Fermi energy of $E_{\rm F} = 0.1$ eV, a carrier mobility of $\mu_{\rm M} = 10^4$ cm^2/Vs, are separated by $d = 0.1$ nm and are free standing in vacuum.

In Fig. 3.2(a), we show the photon count for the structure described above. It is clear

that the count is enhanced with the addition of a graphene sheet, and that both the count and resonant frequencies change as we increase the number of sheets. As shown in Sec. 2.3.1, this occurs due to the hybridization of the graphene sheets, creating an optical mode that is blue-shifted. Figure 3.2(b) shows the corresponding Purcell enhancement, calculated using Eq. (2.53), where we observe that the peaks in Purcell enhancement match the minima of the photon count. This is likely the signature of a larger energy being absorbed by the dipole at those resonances, and therefore the scattering into the far field is weaker.

In Fig. 3.3 we consider the same system as in Fig. 3.2, but the Fermi energy of the sheets is now $E_{\mathrm{F}} = 1$ eV. The plasmon resonances are now more clear and further blue-shifted, highlighting the potential of using the active tunability of graphene to perform frequency sweeps to target a wider range of possible axion masses. As expected, the photon count is also around $10\times$ larger due to effectively reducing the damping through Eq. (2.22), but also because raising the carrier density simply adds more electrons to the plasmon wave and reduces loss to interband transitions.

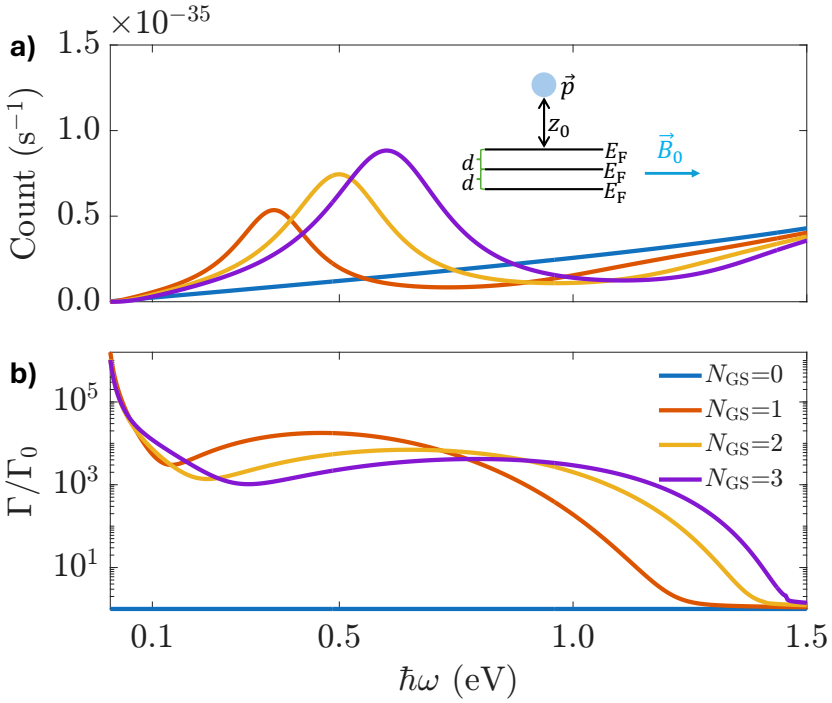

Figure 3.3: Same system as in Fig. 3.2, but the sheets Fermi energy is now $E_{\mathrm{F}} = 1$ eV.

So far, we have considered the dipole placed arbitrarily close to the surface. However, evidence in literature suggests that often there is an optimal position at which the dipole coupling to the surface plasmons underneath is maximal [16]. Therefore, to further enhance the response of the structure, we can likewise determine if there is an optimal height of the probing dipole. Placing it too close to the interface will result in the energy being dissipated into heat, rather than driving a plasmon response. However, it should of course be close enough that the evanescent waves of the dipole reach the interface.

Figure 3.4(a) shows the count of the $N_{\mathrm{GS}} = 2$ system of Fig. 3.3 as a function of

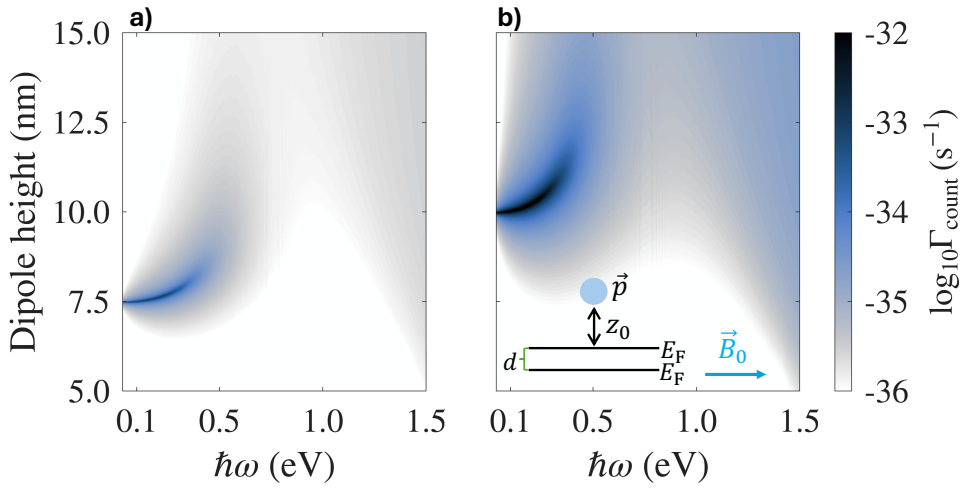

Figure 3.4: **(a)** Photon count for the $N_{\mathrm{GS}} = 2$ system of Fig. 3.3 but with varying height of the dipole z_0 using an effective radius of $r_\alpha = 15$ nm for the dipole. **(b)** Same system but with an effective radius of $r_\alpha = 20$ nm

frequency and height of the dipole z_0. A cut of such plot along the $z_0 = 15$ nm line recovers the results from Fig. 3.3, where we identify a faint resonance around $\hbar\omega \approx 0.5$ eV. However, as we anticipated, as we move the dipole closer to the surface, there is a clear resonance that shifts with the frequency down to $z = 7.5$ nm at $\hbar\omega = 0.1$ eV. Similarly, for Fig. 3.4(b), where the effective radius now is $r_\alpha = 20$ nm (i.e. the bare dipole polarizability is larger by a factor of ~ 2.37), we observe the same qualitative behavior, but converging towards a resonance at $z_0 = 10$ nm. This behavior is accompanied by a larger emission count (2 orders of magnitude), as expected from a dipole with a larger polarizability and therefore larger scattering cross section.

Interestingly, we observe a tendency by which the optimal "height" is approximately given by $z_0 \approx r_\alpha/2$ as the frequency is lowered, independently of the graphene properties. Further analysis reveals that the resonance stems from the denominator of Eq. (2.57), i.e. when

$$\frac{1}{\alpha(r_\alpha)}\mathbb{I} = \frac{\mu_r}{\varepsilon_0}k^2\mathbf{G}(\mathbf{r}_0,\mathbf{r}_0), \tag{3.18}$$

and at frequencies below $\hbar\omega \approx 0.1$ eV, $\mathbf{G}(\mathbf{r}_0,\mathbf{r}_0)$ starts to act as a constant with respect to doping and number of layers. The resonance is then decided by polarizability of the dipole, which is strongly dependent on its effective radius $\alpha \propto r_\alpha^3$.

Despite mild improvements through stack combination and dipole placement, all results in Figs. 3.2–3.4 predict a very small magnitude of the photon count –which means we would have to wait $\approx 10^{17}\times$(the age of the universe) to detect a single photon. In part, this happens because the emission mechanism is not optimized, given that it is proportional to the extinction cross section of the dipole, which sets the "useful" area of the device actually used for photon emission. A clear improvement should come from using more dipoles, such that a larger area of the device is covered, and therefore the emission is enhanced. However, along those lines, an alternative is to use patterned systems that bypass the need for the dipole altogether and can profit from extended size for larger

emission.

3.2.2 Axion Detection in Confined Systems

In Sec. 2.3.1 we saw that graphene ribbons support plasmon modes with $k_{\parallel} = 0$, meaning they can couple directly to the axion-photons. This removes the need for dipole couplers of limited cross section, resulting potentially in a much larger effective area contributing to photon emission. Additionally, we found that the ribbon's response can be approximately described by its polarizability, which, for the first dipolar mode, is given by Eq. (2.37). As such, we can simply use the formulation presented in Sec. 2.4.2 to estimate the field resulting from a ribbon being excited by axions-photons and interacting with the photonic environment.

Figure 3.5 shows the photon count per second and μm (along the ribbon length), using graphene ribbons of varying width and doping. Specifically, we use the same ribbons as in Fig. 2.10, making it clear that the resonances seen in the extinction persist when calculating the photon count. Since the ribbons are excited at a precise frequency and momentum, their resonance are much more sharply defined compared to the extended sheets, which are excited broadly by a dipole. Additionally, we see that the obtained photon counts of the ribbons are up to 10^9 times larger than the ones from the sheet, assuming a realistic ribbon length of 100 μm [37], partly due to switching from a broadband to a precision search, but also because we now get the contribution of the ribbon length.

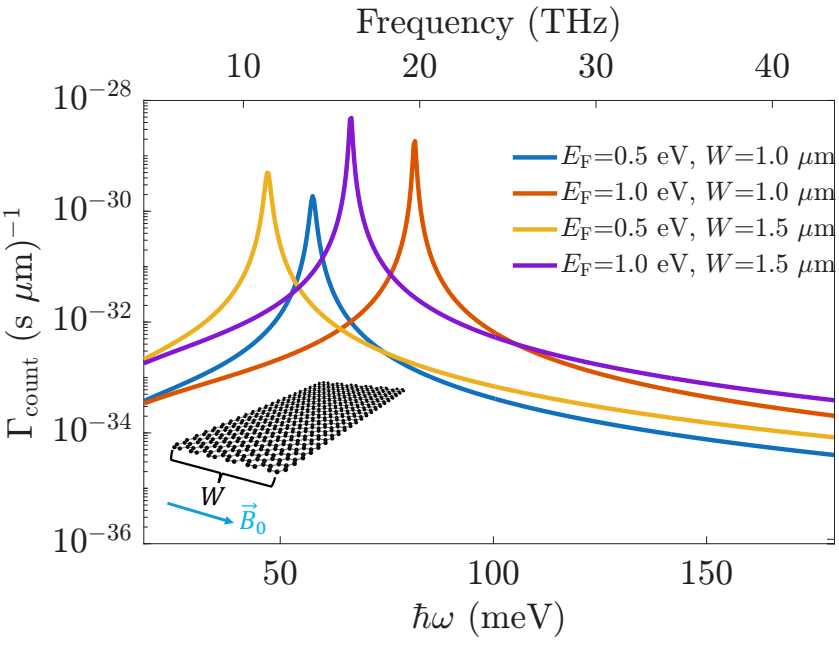

Figure 3.5: The photon count as a result of a free standing graphene ribbon, of width W, interacting with the axion-photons generated through the external magnetic field $\mathbf{B}_0$. We used a carrier mobility of $\mu_{\mathrm{M}} = 10^4$ cm^2/Vs and the local Drude conductivity model.

Just as with the extended graphene sheet, we want to optimize the ribbon system,

as there are many parameters still available to tune. In particular, results from Fig. 3.4 suggest that the vertical placement of the ribbon is a crucial one. Figure 3.6 shows the photon count from a ribbon suspended over some substrate for various heights. We test, as substrates, a graphene sheet, a gold surface, and a combined graphene on gold heterostructure. It is clear that the combination of the material used and the placement of the ribbon affects the count, leaving room for optimization.

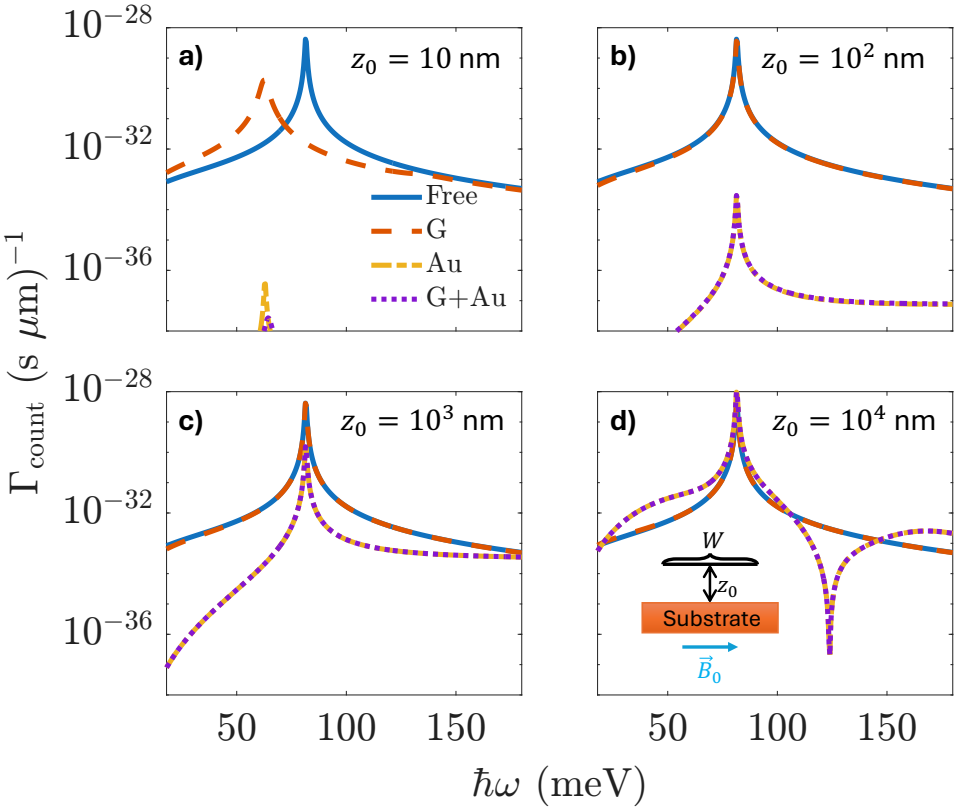

Figure 3.6: Axion-generated photon count for various ribbon-based systems. The blue lines are a free standing ribbon, the orange is with an extended graphene sheet placed at $z = 0$ nm, the yellow is using bulk gold as the second material and the purple is using both an extended graphene sheet and bulk gold, separated by $d = 1$ nm. The ribbon had a width of $W = 1$ μm, a doping of $E_{\text{F}} = 1$ eV and is placed at a distance z_0 above the interface, specifically **(a)** $z_0 = 10$ nm, **(b)** $z_0 = 10^2$ nm, **(c)** $z_0 = 10^3$ nm, and **(d)** $z_0 = 10^4$ nm.

3.2.3 Possible Directions for Count Improvement

Figure 3.7(a) shows the photon count of a graphene sheet as a function of axion-photon coupling and frequency, while Fig 3.7(b) shows the count per micron for a ribbon. It is clear that, even for stronger couplings (that have already been ruled out by other axion-detection experiments or observations, as seen in Fig. 3.1), we need to drastically improve the count for this detection scheme to be viable. For the ribbon system, which currently

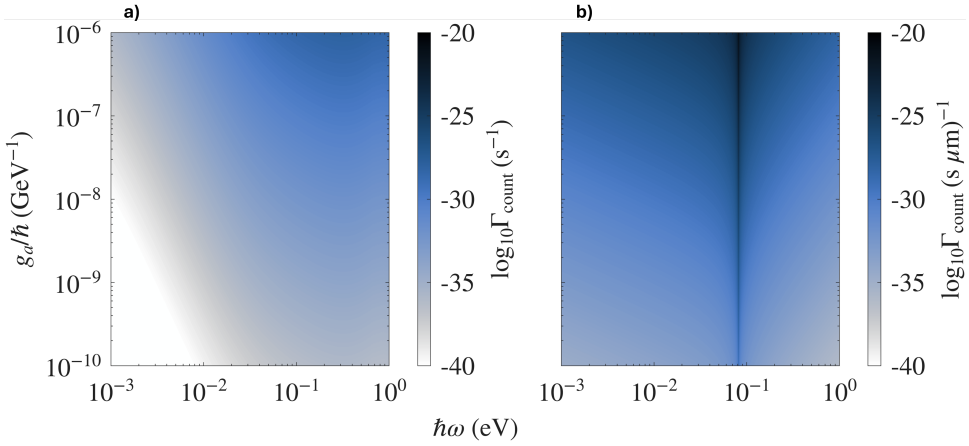

Figure 3.7: **(a)** Photon count emitted per second for a self-standing graphene sheet. **(b)** Photon count emitted per second per micron, for a self-standing ribbon of width $W = 1$ μm. Both strucutres had a Fermi energy $E_{\text{F}} = 1$ eV and a carrier mobilitry of $\mu_{\text{M}} = 10^4$ cm^2/Vs.

outperforms the extended sheet setup, this could be done by increasing the interacting area, e.g adding multiple graphene ribbons [38] or using large "grids" of graphene, which can reach sizes of 2×2 mm [39, 40]. With these, one could maximize the interacting area while still allowing for confined plasmon modes. It has also been shown that periodic arrays of graphene nanostructures, such as graphene disks [41], can provide a larger response. However, this would target a specific axion mass for a given structure (that would be fixed by the array period) and is therefore less flexible.

Alternatively, we could improve the original system of an extended sheet by adding additional scatterers, effectively increasing the area of interaction. This could be done by simply covering the surface in nanospheres or using ordered gold nanostructures [42]. A more advanced solution is to engineer a metasurface scatterer, such that our "probing tip" is no longer a simple dipole, but some efficient scatterer with a much larger cross section, going into the millimeter-squared region [43].

Finally, it should be emphasized that the systems considered here are quite simple, and that a realistic detection experiment would likely combine multiple enhancement methods, combined with additional strategies to lower the detection count floor, such as heterodyne detection, to reach reasonable count values.

Chapter 4

Conclusion

The aim of this work was to develop a theoretical framework for assessing the potential to use nanophtonics to probe axions in the THz region, using GSPPs in nanostructures. To this end, we in Chapter 2 first reviewed the appropriate electrodynamics and studied the behavior of SPPs and GSPPs, demonstrating how the plasmon response of extended graphene can be captured in the Fresnel coefficients through its surface conductivity. We then used this to develop a Green's function machinery, allowing us to calculate the electric field of arbitrary layered structures with translational invariance, for both extremely localized and delocalized sources.

In Chapter 3 we saw how the existence of the axion would modify the Maxwell equations, and that, in the presence of a strong magnetic field, the axions could be treated as a photon source. With this established, we were able to calculate the dipole-assisted photon count of graphene systems of varying complexity, finding that, while the graphene did enhance the count and allowed for tunability, the photon count was of the order 10^{-36} counts pr. second, which limits its potential for this specific application.

In an effort to improve upon this, we examined the enhancement provided by a confined system, specifically using graphene ribbons. Since these can directly interact with the axion-photons, the mediating dipole is unnecessary, and, therefore, the total length of the ribbons is able to directly contribute to photon emission. Remarkably, we found that ribbons are able to achieve up to 10^7 timers larger count pr. micron ribbon length, than for the extended system, which is a promising results since ribbons in excess of 100 μm have been realized experimentally, and many of them can be combined in a sample to achieve an even larger value.

Despite such improvements, the overall photon counts predicted in this work are still too low for the system to be potentially viable for an experiment, which motivated a discussion on possible ways to improve the count. Specifically, a more comprehensive analysis of graphene ribbons and multi-ribbon/grid systems should be pursued, as the active tunability of these systems is quite appealing for axion mass sweeps.

Appendix A

Transfer Matrices for Stratified Media

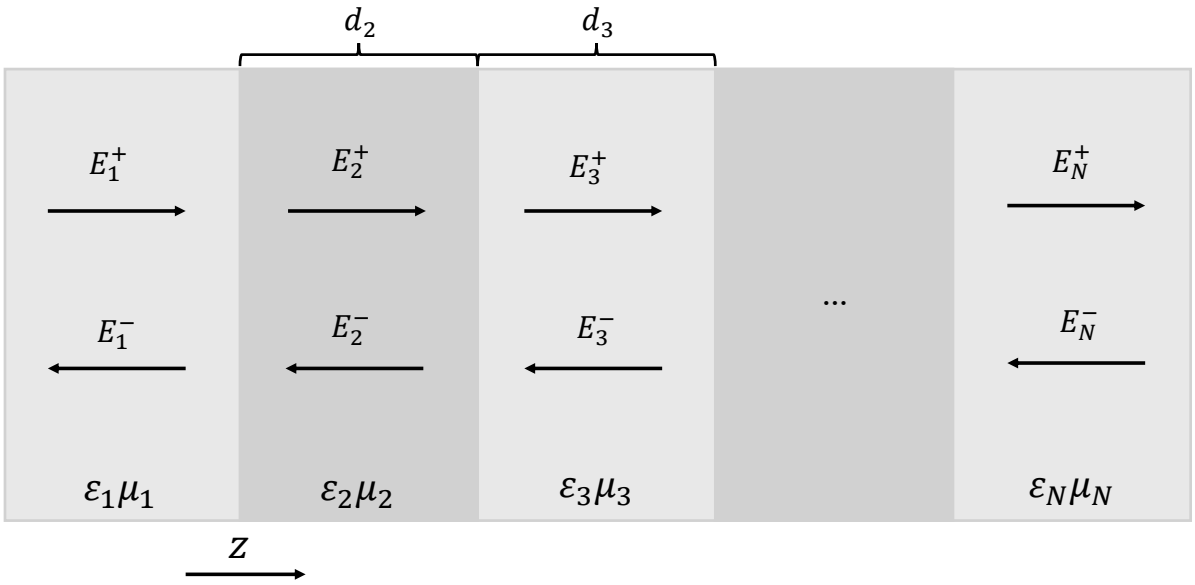

Figure A.1: Schematic of the stacked system used to derive the transfer matrix method (TMM). In each layer i there is the superposition of a forward- E_i^+ and backward-propagating field E_i^- along z. Intermediate layers have a thickness d_i. At each boundary, the fields are matched such that they fulfill the Maxwell boundary conditions in Eqs. (2.10).

We derive the transfer matrix method (TMM) that determines how light is scattered by a multilayered structure of N planar layers, as shown in Fig. A.1. We label layers $i = 1, \cdots, N$, with corresponding thickness d_i (for $i = 2, \cdots, N-1$). Furthermore, we consider that the electric field in each layer can be written as the superposition of upward and downward propagating waves along the z direction, whose amplitudes are respectively written as E_i^+ and E_i^-.

To start, we consider how the fields in the first medium $i = 1$ are related to those in

the second medium $i = 2$. The forward propagating field in medium 2 is given by

$$E_2^+ = t_{12}E_1^+ + r_{21}E_2^-, \tag{A.1}$$

where the first term comes from the field propagating through the interface, the second comes from reflecting off of it (hence the order of the indices), and where t_{12} and r_{12} are the single-interface Fresnel coefficients given by Eq. (2.14) or (2.16), depending on polarization. In general, these admit the presence of a surface conductivity at the interface. Likewise, we find an expression for E_1^-, the downward propagating field in medium $i = 1$, as

$$E_1^- = r_{12}E_1^+ + t_{21}E_2^-. \tag{A.2}$$

Isolating E_1^+ from Eq. (A.1) and introducing it into Eq. (A.2) gives us an expression for E_1^- in terms of the fields $E_2^\pm$

$$E_1^+ = \frac{1}{t_{12}}E_2^+ - \frac{r_{21}}{t_{12}}E_2^-, \tag{A.3}$$

and inserting E_1^- into Eq. (A.2) gives us E_1^- in terms of $E_2^\pm$

$$E_1^- = \frac{r_{12}}{t_{12}}E_2^+ + \left(t_{21} - \frac{r_{12}r_{21}}{t_{12}}\right)E_2^-. \tag{A.4}$$

We can now write the matrix equation connecting the fields in medium 1 to the fields in medium 2

$$\begin{pmatrix} E_1^+ \\ E_1^- \end{pmatrix} = \mathbf{M}_{1,2}\begin{pmatrix} E_2^+ \\ E_2^- \end{pmatrix}, \tag{A.5}$$

where

$$\mathbf{M}_{i,i+1} = \frac{1}{t_{i,i+1}}\begin{pmatrix} 1 & -r_{i+1,i} \\ r_{i,i+1} & t_{i,i+1}t_{i+1,i} - r_{i,i+1}r_{i+1,i} \end{pmatrix}, \tag{A.6}$$

is the transfer matrix connecting medium i and $i + 1$, written in terms of the Fresnel coefficients derived in Sec. 2.1.2 . As the wave propagates through the medium i, it will additionally acquire a phase that we account for through the propagation matrix

$$\mathbf{P}_i = \begin{pmatrix} \mathrm{e}^{-\mathrm{i}k_{zi}d_i} & 0 \\ 0 & \mathrm{e}^{\mathrm{i}k_{iz}d_i}, \end{pmatrix} \tag{A.7}$$

where $k_{zi}^2 = \omega^2/c_i'^2 - k_\parallel^2$ is the out of plane wavevector in medium i, $c_i' = c/n_i$ is the speed of light in medium i and d_i is the thickness of the layer i. The total transfer matrix, connecting medium $i = 1$ with medium $i = N$, is then

$$\mathbf{M}_{1,N}^{\mathrm{tot}} = \mathbf{M}_{1,2}\prod_{i=2}^{N-1}\mathbf{P}_i\mathbf{M}_{i,i+1}. \tag{A.8}$$

The first matrix, $\mathbf{M}_{1,2}$, connects the fields over the first interface. Then the propagation matrix "transfers" the field to the next interface where the next transfer matrix is then calculated, and so on.

Assuming that there is no backward incidence (i.e., $E_N^- = 0$), the relation between the initial fields and the final ones can now be written as

$$\begin{pmatrix} E_1^+ \\ E_1^- \end{pmatrix} = \mathbf{M}_{1,N}^{\text{tot}} \begin{pmatrix} E_N^+ \\ 0 \end{pmatrix} = \begin{pmatrix} m_{11} & m_{12} \\ m_{21} & m_{22} \end{pmatrix} \begin{pmatrix} E_N^+ \\ 0 \end{pmatrix}, \tag{A.9}$$

such that the total transmission and reflection coefficients of the full stack are given by

$$t_{1,N}^{\text{tot}} = \frac{E_N^+}{E_1^+} = \frac{1}{m_{11}}, \tag{A.10a}$$

$$r_{1,N}^{\text{tot}} = \frac{E_1^-}{E_1^+} = \frac{m_{21}}{m_{11}}. \tag{A.10b}$$

A.1 Phase Safe TMM

The method outlined above is fast and precise, but, in practice, it can struggle with larger structures. We note, for example, the negative phase of Eq. (A.7),

$$P_{11,i} = \mathrm{e}^{-\mathrm{i}k_{zi}d_i}. \tag{A.11}$$

When considering fields outside the light cone, i.e. $\mathrm{Im}\{k_{zi}\} > 0$, we get an exponentially increasing function that scales with the in plane momentum and the thickness of the layer. In most programming languages, this leads to integer overflow when $\mathrm{Im}\{k_{zi}\}d_i \approx 710$, which is not unrealistic to pass. As such, we must change our approach slightly. Consider an arbitrary term in the product of Eq. (A.8)

$$\begin{aligned} \mathbf{P}_a\mathbf{M}_{a,b} &= \begin{pmatrix} \mathrm{e}^{-\mathrm{i}k_{za}d_a} & 0 \\ 0 & \mathrm{e}^{\mathrm{i}k_{za}d_a} \end{pmatrix} \begin{pmatrix} 1/t_{a,b} & -r_{b,a}/t_{a,b} \\ r_{a,b}/t_{a,b} & t_{b,a} - r_{a,b}r_{b,a} \end{pmatrix} \\ &= \mathrm{e}^{-\mathrm{i}k_{za}d_a} \begin{pmatrix} 1/t_{a,b} & -r_{b,a}/t_{a,b} \\ \mathrm{e}^{2\mathrm{i}k_{za}d_a}r_{a,b}/t_{a,b} & \mathrm{e}^{2\mathrm{i}k_{za}d_a}(t_{b,a} - r_{a,b}r_{b,a}) \end{pmatrix} \\ &= \frac{1}{P_a}\tilde{\mathbf{M}}_{a,b}, \end{aligned} \tag{A.12}$$

where $P_a = \exp(\mathrm{i}k_{za}d_a)$. Defining the transfer matrix as

$$\tilde{\mathbf{M}}_{i,i+1} \equiv \begin{pmatrix} 1/t_{i,i+1} & -r_{i+1,i}/t_{i,i+1} \\ \mathrm{e}^{2\mathrm{i}k_{zi}d_i}r_{i,i+1}/t_{i,i+1} & \mathrm{e}^{2\mathrm{i}k_{zi}d_i}(t_{i+1,i} - r_{i,i+1}r_{i+1,i}) \end{pmatrix}, \tag{A.13}$$

we ensure that the matrix is always well defined. It then remains to be seen if any of the finale expressions depend on $1/P$, or P which would then converge fine. We can now write the total transfer matrix as

$$\mathbf{M}_{1,N}^{\text{tot}} = \frac{1}{P}\tilde{\mathbf{M}}_{1,N}^{\text{tot}}, \tag{A.14}$$

where

$$P = \prod_{i=2}^{N-1} \mathrm{e}^{\mathrm{i}k_{zi}d_i}, \tag{A.15}$$

and

$$\tilde{\mathbf{M}}_{1,N}^{\text{tot}} = \mathbf{M}_{1,2} \prod_{i=2}^{N-1} \tilde{\mathbf{M}}_{i,i+1} \tag{A.16}$$

As before, we can get the total reflection and transmission coefficients by connecting the amplitude of the initial and final waves

$$\begin{pmatrix} E_1^+ \\ E_1^- \end{pmatrix} = \frac{1}{P}\tilde{\mathbf{M}}_{1,N}^{\text{tot}} \begin{pmatrix} E_N^+ \\ 0 \end{pmatrix} = \frac{1}{P} \begin{pmatrix} \tilde{m}_{11} & \tilde{m}_{12} \\ \tilde{m}_{21} & \tilde{m}_{22} \end{pmatrix} \begin{pmatrix} E_N^+ \\ 0 \end{pmatrix}, \tag{A.17}$$

and we can extract the total transmission and reflection coefficients

$$t_{1,N}^{\text{tot}} = \frac{P}{\tilde{m}_{11}}, \tag{A.18a}$$

$$r_{1,N}^{\text{tot}} = \frac{\tilde{m}_{21}}{\tilde{m}_{11}}. \tag{A.18b}$$

Next, we find the "backwards" coefficients, which describe the transmission or reflection of a wave traveling in the opposite direction through the same structure. The initial and final fields are related by

$$\begin{pmatrix} 0 \\ E_1^- \end{pmatrix} = \frac{1}{P}\tilde{\mathbf{M}}_{1,N}^{\text{tot}} \begin{pmatrix} E_N^+ \\ E_N^- \end{pmatrix}, \tag{A.19}$$

or inversely

$$\begin{pmatrix} E_N^+ \\ E_N^- \end{pmatrix} = \frac{P}{\tilde{m}_{11}\tilde{m}_{22} - \tilde{m}_{12}\tilde{m}_{21}} \begin{pmatrix} \tilde{m}_{22} & -\tilde{m}_{12} \\ -\tilde{m}_{21} & \tilde{m}_{11} \end{pmatrix} \begin{pmatrix} 0 \\ E_1^- \end{pmatrix}, \tag{A.20}$$

such that the coefficients are

$$t_{N,1}^{\text{tot}} = \frac{\tilde{m}_{11}\tilde{m}_{22} - \tilde{m}_{12}\tilde{m}_{21}}{P\tilde{m}_{11}}, \tag{A.21a}$$

$$r_{N,1}^{\text{tot}} = -\frac{\tilde{m}_{12}}{\tilde{m}_{11}}. \tag{A.21b}$$

Due to the $1/P$ factor in $t_{N,1}^{\text{tot}}$, this coefficient appears at first to diverge. However this is not the case: if we write the $\tilde{m}$ matrix elements in as the original matrix elements, we get

$$\begin{aligned} t_{N,1}^{\text{tot}} &= \frac{\tilde{m}_{11}\tilde{m}_{22} - \tilde{m}_{12}\tilde{m}_{21}}{P\tilde{m}_{11}} \\ &= \frac{1}{P\tilde{m}_{11}}\Big(m_{11}m_{22}P^2 - m_{12}m_{21}P^2\Big) \\ &= \frac{P}{\tilde{m}_{11}}\det\Big(\mathbf{M}_{1,N}^{\text{tot}}\Big). \end{aligned} \tag{A.22}$$

Next, we use that $\det(\mathbf{AB}) = \det(\mathbf{A})\det(\mathbf{B})$ and that $\det(\mathbf{P}) = 1$ to obtain

$$t_{N,1}^{\text{tot}} = \frac{P}{\tilde{m}_{11}}\det(\mathbf{M}_{1,2}) \prod_{i=2}^{N-1} \det(\mathbf{M}_{i,i+1}). \tag{A.23}$$

Finally, using the fact that the determinant of a single interface transfer matrix is just the ratio of transmission coefficients, $\det(\mathbf{M}_{a,b}) = t_{b,a}/t_{a,b}$, the total backwards transmission coefficient can be written as

$$t_{N,1}^{\text{tot}} = \frac{P}{\tilde{m}_{11}} \prod_{i=1}^{N-1} \frac{t_{i+1,i}}{t_{i,i+1}}. \tag{A.24}$$

This slightly modified approach to the traditional TMM therefore yields the same scattering coefficients, while avoiding the need to evaluate potential numerically problematic phases.

Declaration of AI use

In this work AI was not used for writing or generating any results. However, the LLM *Gemini* was used for optimizing and debugging code. We also sporadically used it to discuss theory and it motivated the theory developed in Appendix A.1.

Bibliography

[1] Gerardt Hooft. Symmetry breaking through bell-jackiw anomalies. *Physical Review Letters*, 37:8–11, 1976.

[2] Hai-Yang Cheng. The strong cp problem revisited. *Physics Reports*, 158(1):1–89, 1988.

[3] Roberto D Peccei and Helen R Quinn. Cp conservation in the presence of pseudoparticles. *Physical Review Letters*, 38(25):1440, 1977.

[4] Steven Weinberg. A new light boson? *Physical Review Letters*, 40(4):223, 1978.

[5] Frank Wilczek. Problem of strong p and t invariance in the presence of instantons. *Physical Review Letters*, 40(5):279, 1978.

[6] Francesca Chadha-Day, John Ellis, and David JE Marsh. Axion dark matter: What is it and why now? *Science advances*, 8(8):eabj3618, 2022.

[7] John Preskill, Mark B Wise, and Frank Wilczek. Cosmology of the invisible axion. *Physics Letters B*, 120(1-3):127–132, 1983.

[8] David J Griffiths. *Introduction to electrodynamics*. Cambridge University Press, 2023.

[9] Lukas Novotny and Bert Hecht. *Principles of nano-optics*. Cambridge university press, 2012.

[10] Ulrich Hohenester. *Nano and Quantum Optics*. Springer, 2020.

[11] Eduardo José Machado Correia Brioso Dias. *Nanoscale manipulation of optical fields*. PhD thesis, Universitat Politècnica de Catalunya, 2022.

[12] Theis Pilegaard Rasmussen. *Directing Nanoscale Light-Matter Interactions with Polaritons in Low-Dimensional Systems*. PhD thesis, SDU, Denmark, 2024.

[13] Chi-Fan Chen, Cheol-Hwan Park, Bryan W. Boudouris, Jason Horng, Baisong Geng, Caglar Girit, Alex Zettl, Michael F. Crommie, Rachel A. Segalman, Steven G. Louie, and Feng Wang. Controlling inelastic light scattering quantum pathways in graphene. *Nature*, 471(7340):617–620, 2011.

[14] Hongtao Liu, Yunqi Liu, and Daoben Zhu. Chemical doping of graphene. *Journal of materials chemistry*, 21(10):3335–3345, 2011.

[15] F. J. García de Abajo. Graphene plasmonics: challenges and opportunities. *ACS Photonics*, 1(3):135–152, 2014.

[16] Frank H. L. Koppens, Darrick E. Chang, and F. J. García de Abajo. Graphene plasmonics: a platform for strong light–matter interactions. *Nano Lett.*, 11(8):3370–3377, 2011.

[17] Paulo André Dias Gonçalves and Nuno M. R. Peres. *An introduction to graphene plasmonics*. World Scientific, 2016.

[18] B Wunsch, T Stauber, F Sols, and Francisco Guinea. Dynamical polarization of graphene at finite doping. *New Journal of Physics*, 8(12):318–318, 2006.

[19] Neil W Ashcroft, N David Mermin, et al. Solid state physics, 1976.

[20] Renwen Yu, Luis M Liz-Marzán, and F Javier García de Abajo. Universal analytical modeling of plasmonic nanoparticles. *Chemical Society Reviews*, 46(22):6710–6724, 2017.

[21] D. N. Basov, M. M. Fogler, and F. J. García de Abajo. Polaritons in van der waals materials. *Science*, 354(6309):aag1992, 2016.

[22] P. A. D. Gonçalves, E. J. C. Dias, Sanshui Xiao, M. I. Vasilevskiy, N. Asger Mortensen, and N. M. R. Peres. Graphene plasmons in triangular wedges and grooves. *ACS Photonics*, 3(11):2176–2183, 2016.

[23] Sergey G. Menabde, Jacob T. Heiden, Joel D. Cox, N. Asger Mortensen, and Min Seok Jang. Image polaritons in van der waals crystals. *Nanophotonics*, 11(11):2433–2452, 2022.

[24] Thomas Christensen, Wei Yan, Antti-Pekka Jauho, Martijn Wubs, and N. Asger Mortensen. Kerr nonlinearity and plasmonic bistability in graphene nanoribbons. *Phys. Rev. B*, 92(12):121407, 2015.

[25] Renwen Yu, Joel D. Cox, J. R. M. Saavedra, and F. J. García de Abajo. Analytical modeling of graphene plasmons. *ACS Photonics*, 4(12):3106–3114, 2017.

[26] Eduardo JC Dias, A Rodríguez Echarri, Theis P Rasmussen, F Javier García de Abajo, and Joel D Cox. Active steering of cathodoluminescence through a generalized smith–purcell effect. *Light: Science & Applications*, 15(1):218, 2026.

[27] LA Blanco and FJ García De Abajo. Spontaneous light emission in complex nanostructures. *Physical review B*, 69(20):205414, 2004.

[28] Ciaran O'Hare. cajohare/axionlimits: Axionlimits. https://cajohare.github.io/AxionLimits/, July 2020.

[29] Pierre Sikivie. Experimental tests of the" invisible" axion. *Physical Review Letters*, 51(16):1415, 1983.

[30] H Terças, JD Rodrigues, and JT Mendonça. Axion-plasmon polaritons in strongly magnetized plasmas. *Physical Review Letters*, 120(18):181803, 2018.

[31] Jonathan Ouellet and Zachary Bogorad. Solutions to axion electrodynamics in various geometries. *Physical Review D*, 99(5):055010, 2019.

[32] Alexander J Millar, Georg G Raffelt, Javier Redondo, and Frank D Steffen. Dielectric haloscopes to search for axion dark matter: Theoretical foundations. *Journal of Cosmology and Astroparticle Physics*, 2017(01):061–061, 2017.

[33] LD Landau and EM Lifshitz. The classical theory of fields, 4th edn., vol. 2, 1980.

[34] Justin I Read. The local dark matter density. *Journal of Physics G: Nuclear and Particle Physics*, 41(6):063101, 2014.

[35] Jesse Liu, Kristin Dona, Gabe Hoshino, Stefan Knirck, Noah Kurinsky, Matthew Malaker, David W Miller, Andrew Sonnenschein, Mohamed H Awida, Peter S Barry, et al. Broadband solenoidal haloscope for terahertz axion detection. *Physical Review Letters*, 128(13):131801, 2022.

[36] Younggeun Kim, Dongok Kim, Junu Jeong, Jinsu Kim, Yun Chang Shin, and Yannis K Semertzidis. Effective approximation of electromagnetism for axion haloscope searches. *Physics of the Dark Universe*, 26:100362, 2019.

[37] Nicolas Camara, Benoit Jouault, Bilal Jabakhanji, Alessandra Caboni, Antoine Tiberj, Christophe Consejo, Philipe Godignon, and Jean Camassel. Multidimensional characterization, landau levels and density of states in epitaxial graphene grown on sic substrates. *Nanoscale research letters*, 6(1):141, 2011.

[38] Theis P. Rasmussen, Álvaro Rodríguez Echarri, F. J. García de Abajo, and Joel D. Cox. Nonlocal and cascaded effects in nonlinear graphene nanoplasmonics. *Nanoscale*, 15(7):3150–3158, 2023.

[39] Yijia He, Junchao Lao, Tingting Yang, Xiao Li, Xiaobei Zang, Xinming Li, Miao Zhu, Qiao Chen, Minlin Zhong, and Hongwei Zhu. Galvanism of continuous ionic liquid flow over graphene grids. *Applied Physics Letters*, 107(8), 2015.

[40] Tingting Yang, Wen Wang, Hongze Zhang, Xinming Li, Jidong Shi, Yijia He, Quanshui Zheng, Zhihong Li, and Hongwei Zhu. Tactile sensing system based on arrays of graphene woven microfabrics: electromechanical behavior and electronic skin application. *ACS nano*, 9(11):10867–10875, 2015.

[41] Juan R Deop-Ruano, Stephen Sanders, Alessandro Alabastri, Wilton JM Kort-Kamp, Diego AR Dalvit, and Alejandro Manjavacas. Optical response of periodic arrays of graphene nanodisks. *Physical Review Applied*, 18(4):044071, 2022.

[42] Shuguang Zhang, Xingwang Zhang, and Xin Liu. Electromagnetic enhancement of graphene raman spectroscopy by ordered and size-tunable au nanostructures. *Nanoscale Research Letters*, 10(1):390, 2015.

[43] Dimitrios C Zografopoulos, Antonio Ferraro, José Francisco Algorri, Pedro Martín-Mateos, Braulio García-Cámara, Aldo Moreno-Oyervides, Viktor Krozer, Pablo Acedo, Ricardo Vergaz, José Manuel Sánchez-Pena, et al. All-dielectric silicon metasurface with strong subterahertz toroidal dipole resonance. *Advanced Optical Materials*, 7(19):1900777, 2019.